Mon. Not. R. Astron. Soc. **302,** 209–221 (1999)

# X-ray luminosities for a magnitude-limited sample of early-type galaxies from the *ROSAT* All-Sky Survey

J. Beuing,[1⋆] S. Döbereiner,[2] H. Böhringer[2] and R. Bender[1]
[1] *Universitäts-Sternwarte München, Scheinerstrasse 1, D-81679 München, Germany*
[2] *Max-Planck-Institut für Extraterrestrische Physik, D-85740 Garching bei München, Germany*

Accepted 1998 August 3. Received 1998 June 1; in original form 1997 December 30

**ABSTRACT**

For a magnitude-limited optical sample ($B_T \leq 13.5$ mag) of early-type galaxies, we have derived X-ray luminosities from the *ROSAT* All-Sky Survey. The results are 101 detections and 192 useful upper limits in the range from $10^{36}$ to $10^{44}$ erg s$^{-1}$. For most of the galaxies no X-ray data have been available until now. On the basis of this sample with its full sky coverage, we find no galaxy with an unusually low flux from discrete emitters. Below $\log(L_B) \approx 9.2$ L$_\odot$ the X-ray emission is compatible with being entirely due to discrete sources. Above $\log(L_B) \approx 11.2$ L$_\odot$ no galaxy with only discrete emission is found. We further confirm earlier findings that $L_x$ is strongly correlated with $L_B$. Over the entire data range the slope is found to be 2.23($\pm$0.12). We also find a luminosity dependence of this correlation. Below $\log L_x = 40.5$ erg s$^{-1}$ it is consistent with a slope of 1, as expected from discrete emission. Above this value the slope is close to 2, as expected from gaseous emission. Comparing the distribution of X-ray luminosities with the models of Ciotti et al. leads to the conclusion that the vast majority of early-type galaxies are in the wind or outflow phase. Some of the galaxies may have already experienced the transition to the inflow phase. They show X-ray luminosities in excess of the value predicted by cooling flow models with the largest plausible standard supernova rates. A possible explanation for these super X-ray-luminous galaxies is suggested by the smooth transition in the $L_x$–$L_B$ plane from galaxies to clusters of galaxies. Gas connected to the group environment might cause the X-ray overluminosity.

**Key words:** surveys – X-rays: galaxies.

## 1 INTRODUCTION

The launch of the *Einstein* observatory in 1978 provided for the first time the possibility of studying X-ray properties of galaxies. Fabbiano, Kim & Trinchieri (1991) constructed a large homogeneous sample of X-ray data for early-type galaxies from the *Einstein* data bank. Their sample comprises 70 detections and 78 upper limits. It is composed of all bright galaxy targets of *Einstein* observations, and all other galaxies in the Revised Shapley–Ames Catalogue (RSA, Sandage 1981) and Second Reference Catalogue of Bright Galaxies (RC2, de Vaucouleurs et al. 1976) serendipitously included in the *Einstein* fields. This sample might therefore be subject to selection biases.

The aim of this work is to derive a homogeneous set of X-ray luminosities with well-defined properties, as free of selection biases as possible. The *ROSAT* All-Sky Survey (RASS) provides an ideal basis for such an analysis (Trümper 1993). To achieve this goal our investigation is based on an optically selected magnitude-limited sample ($B_T \leq 13.5$ mag) of early-type galaxies with corresponding X-ray data from the RASS with its full sky coverage. Our sample is intended to serve as a firm basis for statistical analysis of various X-ray properties of early-type galaxies, as well as to search for galaxies not detected in X-rays so far.

In Section 2 we specify the optical sample. Section 3 describes the reduction steps applied to the raw data. In Section 4 we present the results, compare our findings with the literature, specify basic properties of the X-ray emission associated with galaxies, and compare them with current theories. Section 5 summarizes the results.

## 2 THE OPTICAL SAMPLE

The optical sample consists of two subsamples. The southern part was selected for the ESO key project 'towards a physical classification of early-type galaxies' (Bender et al. 1989). It contains all E and E/S0 galaxies south of $\delta = 0°$ and brighter than $B_T = 13.5$ mag of the 7 Samurai list (Faber et al. 1989), and all objects from the ESO Lauberts–Valentijn Catalogue (Lauberts & Valentijn 1989, ESO/LV hereafter) brighter than $B_T = 13.5$ mag with morphological type $T_{old}$ or $T_{new} \leq -3$. The northern part contains all E and E/S0 galaxies brighter than $B_T = 13.5$ mag from the 7 Samurai list with $\delta \geq 0°$. Further galaxies brighter than $B_T = 13.7$ mag, with

⋆E-mail: beuing@usm.uni-muenchen.de

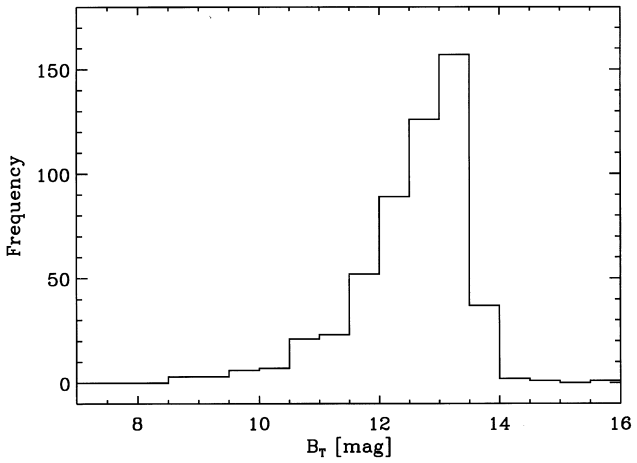


**Figure 1.** Distribution of total blue magnitudes $B_T$ (not corrected for galactic extinction) in the total sample according to RC3.

$\delta \geq 0^\circ$ and numerical class $T \leq -3$, were taken from the Third Reference Catalogue of Bright Galaxies (de Vaucouleurs et al. 1991, RC3 hereafter) and the Tully Nearby Galaxies Catalogue (Tully 1988). A slightly fainter value for $B_T$ was chosen, since de Vaulouleurs et al. (1991) found hints for the RC3 being on a marginally fainter system (by $0.12 - 0.18$ mag) than the ESO/LV catalogue. The final sample comprises a total of 530 early-type galaxies, 313 in the southern and 217 in the northern part. 49 per cent are ellipticals ($T = -5$), including one compact elliptical ($T = -6$), 15 per cent cD-type galaxies ($T = -4$), 26 per cent E/S0s ($T = -3$), 7 per cent S0s ($T = -2$) and 3 per cent later types, according to RC3. Judging by the bright end of the distribution, the sample is starting to become incomplete at $B_T \approx 13.0$ mag, but is still complete to roughly 90 per cent at $B_T = 13.5$ mag assuming a homogeneous distribution in space (see Fig. 1). The sample objects can be found in environments ranging from the lowest densities in the field, over loose and small groups, to Hickson compact groups and clusters of galaxies. 11 active galactic nuclei (AGN) from the catalogue of Véron-Cetty & Véron (1996) are identified in the total sample. Besides 'normal' galaxies, a number of disturbed galaxies are also part of the sample.

## 3 DATA REDUCTION

For each of the 530 objects, a field of about $2^\circ \times 2^\circ$ around the galaxy was retrieved from the RASS. The typical exposure time is $\approx$ 400 s. The data were binned to raw count images of $512 \times 512$ pixels in the hard band (0.64–2.36 keV). This yields a scale of 15 arcsec per pixel, a reasonable oversampling compared with the RASS angular resolution. The hard band was chosen to improve the detection efficiency, since the soft band essentially adds background and hence reduces the signal-to-noise ratio. The images were smoothed with a Gaussian function with a FWHM of a typical Position Sensitive Proportional Counter (PSPC) point spread function (PSF). Then X-ray contours were overlaid on to Digital Sky Survey fields to check whether the X-ray emission originates from the galaxy itself, or whether possibly some other X-ray-bright object is responsible for the emission.

### 3.1 Background

Owing to the rather short exposure times, no smooth background is visible in the images and hence it is difficult to derive a local background around the target source. Therefore the background was determined by placing a few hundred circles with a radius of 2.5 arcmin on randomly chosen positions on each frame, avoiding regions with clearly visible bright sources. From the counts in the circles an approximate mean background was calculated. To avoid contribution from faint sources to the background level, all values lying outside a $3\sigma$ range around this value were excluded. From the remaining apertures the final background value was derived.

### 3.2 Source count and count rate extraction

Source counts were extracted from the smoothed images. The counts were integrated in circles of growing radius centred on the X-ray position until the curve of integrated counts reached its flat part. The aim was to include all the counts coming from the galaxy. In some cases the few counts from the galaxy target in combination with the noisy background made it difficult to determine the transition to the flat part. This uncertainty is included in the final error estimate.

For some objects it was not clear whether some (clumpy) emission belongs to the source or is associated with a background or foreground source. In these cases the mean value between the source with and without this suspicious emission was calculated. The uncertainties arising from this procedure were also included in the errors. After correcting the images for vignetting and exposure, count rates were extracted.

The criterion for detection was that of a signal-to-noise ratio of at least $3\sigma$ above the background, assuming $\mathrm{S/N} = S/\sqrt{S+B}$ ($S$ = source counts, $B$ = background counts). For all other objects in the sample we derived $3\sigma$ upper limits above the background. The upper limits were calculated within a circle of radius three optical half-light radii. The bulk of the optical flux is contained in this circle and, since optical and X-ray surface brightnesses roughly decline in proportion to one another (Trinchieri, Fabbiano & Canizares 1986), the bulk of the X-ray emission also falls within this circle. The derived X-ray luminosities are rather insensitive to the exact size of the circle, as the background only contributes a fraction of $\leq 10$ per cent in most cases.

### 3.3 Luminosities

To convert count rates into 0.64–2.36 keV X-ray luminosities, a Raymond–Smith plasma (Raymond & Smith 1977) with a temperature of 1 keV and cosmic abundance (Allen 1973) was assumed. The line-of-sight hydrogen column densities were taken from Dickey & Lockman (1990). Distances were compiled from a variety of catalogues using group velocities from Faber et al. (1989) and Garcia (1993) in the first place, complemented by data from ESO/LV and RC3 and in a few cases from individual sources. Velocities were corrected to the centroid of the Local Group according to the Revised Shapley–Ames Catalogue (Sandage 1981) and converted into distances adopting $H_0 = 50$ km s$^{-1}$ Mpc$^{-1}$. In the few cases where the correction to the centroid of the Local Group gave a negative value, the uncorrected velocity was taken instead. The mean error for the X-ray luminosity arising from the measurement procedure and Poisson noise is of the order of 0.095 dex.

#### *3.3.1 Justification of model assumptions*

The X-ray emission of early-type galaxies mostly originates from a hot interstellar gas (Forman, Jones & Tucker 1985). An additional hard component, often attributed to accreting X-ray binaries, is

most important for galaxies with low-$L_x/L_B$ ratios (e.g. Canizares, Fabbiano & Trinchieri 1987; Kim, Fabbiano & Trinchieri 1992).

Gas temperatures and adundances have been derived by a number of authors. Davis & White (1996) measured temperatures and abundances for a complete sample of elliptical galaxies with *ROSAT*. Of the 43 sample objects, 30 had enough counts to allow temperature determinations. They derived a mean temperature of $\langle T\rangle = 0.98$ keV, applying a single-component isothermal Raymond–Smith plasma. Their measured abundances are notedly subsolar, the mean value being $\langle Z\rangle = 0.28\ Z_\odot$.

However, recent *ASCA* results require at least a two-temperature (component) model. Matsumoto et al. (1997) fitted a two-component model to their data, consisting of a thermal bremsstrahlung model with a fixed temperature of 12 keV for the hard component, plus a thin thermal Raymond–Smith model for the soft component. They derived a mean gaseous temperature of $\langle T\rangle = 0.73$ keV, about 0.25 keV lower than the mean temperature of Davis & White (1996), and a mean abundance of $\langle Z\rangle = 0.29\ Z_\odot$, consistent with Davis & White (1996). More recent results confirm the slightly lower mean temperatures of Matsumoto et al. (1997). Buote & Fabian (1998) re-investigated the spectral properties of ellipticals with *ASCA*. Assuming single-temperature models, they confirmed the earlier results with very subsolar abundances, $\langle Z\rangle = 0.19(\pm 0.12)\ Z_\odot$. However, in almost all cases the single-temperature MEKAL model clearly provides unacceptable fits to the *ASCA* spectra. Applying two-temperature MEKAL (Liedahl, Osterheld & Goldstein 1995) (or Raymond–Smith) models to their data, assuming tied $n_H$ and $Z$, initially did not alter the results significantly, but many fits were not found to be at their global minima. When using a different fitting approach, Buote & Fabian usually obtained a deeper minimum with a reduced $\chi^2$ of $\approx$1. They finally derived abundances much higher than deduced before, namely a mean abundance of $\langle Z\rangle = 0.9(\pm 0.7)\ Z_\odot$. The mean temperature of the cold component, attributed to a phase of hot gas for both the low- and high-$L_x/L_B$ galaxies, is found to be $\langle T\rangle = 0.69$ keV. The hot components in the high-$L_x/L_B$ galaxies have fitted temperatures $\leq$2 keV, consistent with a phase of hot gas, whereas the low-$L_x/L_B$ galaxies have $T \gtrsim 5$ keV, which is consistent with emission from discrete sources. Matsushita et al. (1994) instead found that in X-ray-bright galaxies also a hard component with a temperature of $\gtrsim$2 keV can generally be detected, which is consistent with the integrated emission of discrete X-ray sources. The *ASCA* spectra of this hard component resemble those of bulge-dominated spirals which can be fitted with a thermal bremsstrahlung model with $T \gtrsim 5$ keV (e.g. Makishima et al. 1989).

Summarizing the above results, the X-ray spectra of early-type galaxies require at least two-temperature models. The low-temperature component is consistent with emission from a hot thermal plasma. The two *ASCA* results give a mean gas temperature of about $\langle T\rangle = 0.71$ keV. Davis & White (1996) derived a slightly larger value, but neglecting three galaxies with unusually high temperature, connected with large errors, reduces the mean temperature to $\langle T\rangle = 0.76$ keV. Although significantly subsolar abundances for the gaseous component were measured in the past, the most recent results point towards solar values. However, the abundances of ellipticals can still be considered as uncertain, and have to be investigated further. The high-temperature component ($T \gtrsim 2$ keV) is consistent with the emission from low-mass X-ray binaries, being more important for the low-$L_x/L_B$ galaxies. Some fraction of the galaxies in our sample are expected to be dominated by this emission.

For the reasons mentioned above, we chose to use simply a temperature of $T = 1$ keV in combination with cosmic abundances, and we provide error estimates in the following section.

#### *3.3.2 Error estimates*

How does our choice of $T = 1$ keV and cosmic abundances affect the absolute values of the X-ray luminosities in the 0.64–2.36 keV band? Lowering the temperature of the Raymond–Smith plasma to $T = 0.70$ keV and keeping the cosmic abundance would increase our X-ray luminosities by $\approx$0.18 dex. Taking the mean values as measured by Matsumoto et al. (1997) ($T = 0.73$ keV and $Z = 0.29\ Z_\odot$) results in a decrease of our luminosities by $\approx$0.32 dex, whereas assuming $\langle T\rangle = 0.69$ keV and $\langle Z\rangle = 0.9\ Z_\odot$ (Buote & Fabian 1998) would cause an increase of $\approx$0.14 dex. These error estimates apply to high-$L_x/L_B$ galaxies, in which the X-ray emission is dominated by a thin thermal plasma. The values given above should be regarded as error estimates rather than a mean correction factor, since individual combinations of $T$ and $Z$ can lead to rather different correction factors.

Assuming a thermal bremstrahlung model for the X-ray emission of low-$L_x/L_B$ galaxies leads to an increase of the X-ray luminosity of $\approx$0.1 dex, virtually insensitive to the temperature. The values range from 0.08 dex for $T = 2$ keV to 0.12 dex for an extreme value of $T = 25$ keV.

The validity of these error estimates is presented in Section 4.2, where our data are compared with previous results from *Einstein*, *ROSAT* and *ASCA*.

## 4 RESULTS

### 4.1 Selection criteria/final X-ray sample

The final X-ray sample consists of all normal galaxies showing individual emission as well as galaxies at the centres of clusters/groups, if the X-ray emission is centred on the galaxy and is reasonably symmetric around it. Excluded are galaxies not at the centre but embedded in bright cluster emission, unless they clearly stand out against it (e.g. IC 310 at the edge of the Perseus cluster). This avoids confusion with inhomogeneities or clumpiness of the cluster emission. Upper limits are always omitted in these cases, since they do not give useful values owing to the enhanced background of the bright cluster emission. Upper limits are also rejected from the list, if the mean exposure time falls short of 100 s. In these cases parts of the images hardly show any X-ray emission at all, and hence no reliable values can be derived. Moreover, upper limits were excluded in the case when the galaxies exceeded a distance of 60 Mpc. This limit corresponds to a distance at which an $L^*$ galaxy [$L^* = 3.4 \times 10^{10}\ L_\odot$ or $\log(L_B/L_\odot) = 10.4$] with $\log(L_x) = 41.0$ erg s$^{-1}$ would be detected with a signal-to-noise ratio of 3$\sigma$ above the background, adopting typical values for $n_H$, exposure time and optical extent. The X-ray luminosity adopted locates the $L^*$ galaxy near the boundary between X-ray-bright galaxies possessing a hot gaseous halo and galaxies for which the X-ray emission is likely to be dominated by discrete sources (Kim et al. 1992). This is an arbitrary limit, but including galaxies with increasingly higher distances would give meaningless upper limits.

The results of this study are 101 detections and 192 useful upper limits. Detections of individual galaxies have counts ranging from 10.8 to 14 715 with a median of 51 counts (Fig. 2); the corresponding count rates range from 0.02 to 33 count s$^{-1}$ with a median of 0.13 count s$^{-1}$ in the hard band (Fig. 3). Only 68 galaxies out of 293 in the X-ray sample are included in the *Einstein* sample of Fabbiano

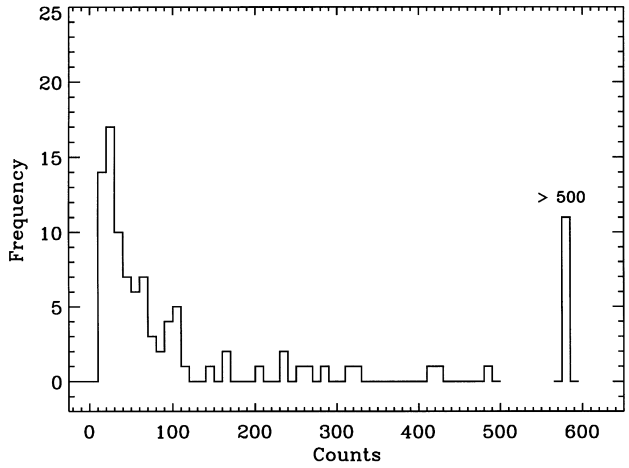


**Figure 2.** Histogram of counts (detections).

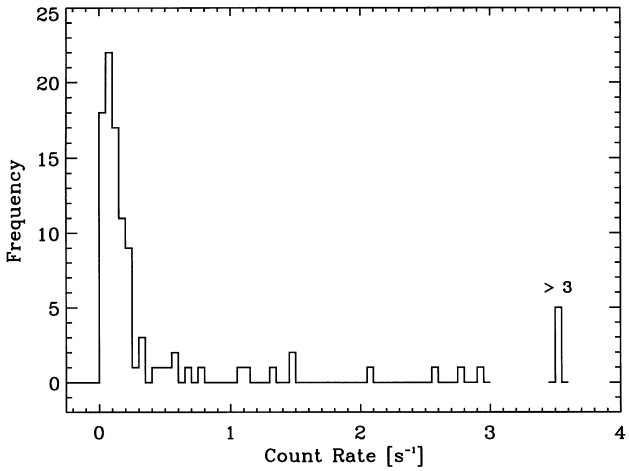


**Figure 3.** Histogram of count rates (detections).

et al. (1992). Fig. 4 shows the histogram of $B_T$ values for the final X-ray sample. It is complete to ≈75 per cent at $B_T = 12.5$ and still to ≈70 per cent at $B_T = 12.75$. All the relevant data are listed in Table 1.

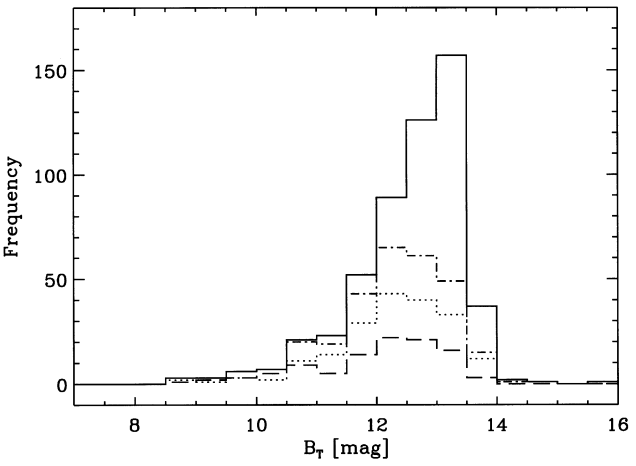


**Figure 4.** Histogram of total blue magnitudes $B_T$ (not corrected for extinction) in the final X-ray sample. The dashed line refers to detections, the dotted line represents upper limits and the dash–dotted line indicates upper limits plus detections. The solid line refers to the total optical sample.

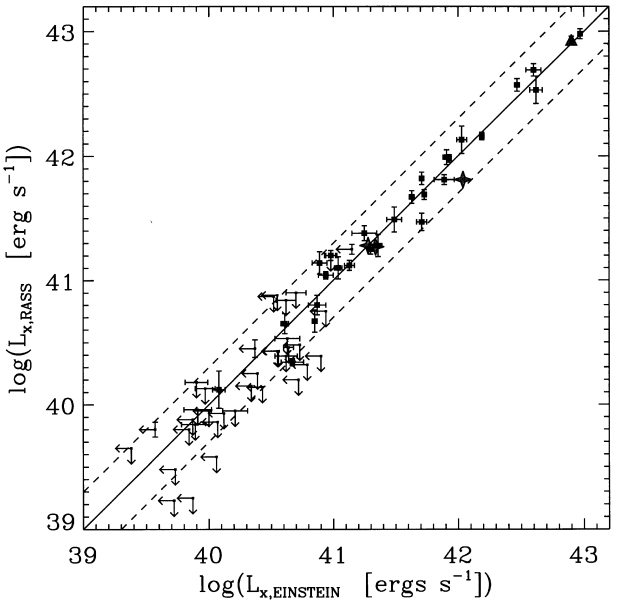


**Figure 5.** Comparison with the 0.2–4.0 keV X-ray luminosities of Fabbiano et al. Fabbiano et al. 1991. Error bars refer to detections; solid arrows represent upper limits. The dashed lines indicate a difference of a factor of 2. X-ray luminosities are corrected for discordant distance estimates and different energy ranges.

### 4.2 Comparison with the literature

*4.2.1 Einstein*

Our luminosities are in good agreement with the *Einstein* luminosities of Fabbiano et al. (1991) (see Fig. 5). Before comparison, the X-ray luminosities were corrected for discordant distance estimates and different energy ranges. The passband correction of 0.084 dex was calculated using a synthetic Raymond–Smith spectrum with a temperature of 1 keV and cosmic abundances. In the few cases for which the difference in detections is about 0.2 dex, it can generally be explained by confusion of the X-ray emission with that of a nearby bright object. One deviating object is an AGN, and the difference may be the result of time variability. Differences in the upper limits are possibly the result of different estimates of the optical extent and hence different areas in which the signal-to-noise ratio is calculated.

*4.2.2 ROSAT*

On average our X-ray luminosities agree to better than a factor of 2 with those of Fabbiano, Kim & Trinchieri (1994, FKT), Fabbiano & Schweizer (1995, FS), Jones et al. (1997, J), Kim & Fabbiano (1995, KF), Kim, Fabbiano & Mackie (1998, KFM), Pildis, Bregman & Evrard (1994, PBE), Rhee, Burns & Kowalski (1994, RBK), Trinchieri, Fabbiano & Kim (1996, TFK) and Trinchieri et al. (1994, TKFC), shown as filled squares in Fig. 6. Excluding the two outliers for reasons discussed below, the scatter around the line of correspondence is ≲0.1 dex. The data are individually corrected for differences in distance and passband, using the same technique as for the comparison with the *Einstein* data. Passband corrections range from 0.04 to 0.17 dex. Only two luminosities depart by more than ≈0.15 dex. In one case, applying an unsuitable model might be the reason for the discrepancy of the X-ray luminosities for the X-ray-faint galaxy NGC 4365. FKT found that a two-temperature model is appropriate to describe the overall spectral distribution.

**Table 1.** Data for the final X-ray sample. The columns are as follows. $T$: numerical type according to RC3; $B_T$: total observed blue magnitude, not corrected for extinction; $D$: distance in Mpc; $\log(L_B)$: total blue luminosity in solar units; $n_H$: hydrogen column density; $R$: radius in which the signal was extracted in arcmin; in the case of upper limits, the radius of three optical half-light radii is given; Counts: source counts; Count rate: source count rate; $\log(L_x)$: X-ray luminosity; upper limits are marked with a prefixed '<'; Error: error of the X-ray luminosity $L_x$ in dex.

| Name | $T$ RC3 | $B_T$ mag | $D$ Mpc | $\log(L_B)$ $L_\odot$ | $n_H$ $10^{-21}$ cm$^{-2}$ | $R$ arcmin | Counts | Count rate s$^{-1}$ | $\log(L_x)$ erg s$^{-1}$ | Error dex |
|---|---|---|---|---|---|---|---|---|---|---|
| ESO 1010140 | -3.0 | 13.01 | 45.08 | 10.61 | 1.410 | 0.750 | 9.06 | 0.08199 | < 41.21 | |
| ESO 1070040 | -4.2 | 12.86 | 59.39 | 10.59 | 0.359 | 0.987 | 9.10 | 0.05035 | < 41.15 | |
| ESO 1090221 | | 12.10 | 56.14 | 10.82 | 0.260 | 1.250 | 9.32 | 0.01974 | < 40.70 | |
| ESO 1380050 | -2.5 | 12.78 | 52.90 | 10.82 | 1.419 | 3.750 | 10.99 | 0.08808 | < 41.38 | |
| ESO 1480170 | -5.0 | 13.26 | 59.70 | 10.41 | 0.329 | 0.752 | 9.07 | 0.02805 | < 40.90 | |
| ESO 1830300 | -2.9 | 12.55 | 52.24 | 10.70 | 0.734 | 0.694 | 9.05 | 0.06714 | < 41.22 | |
| ESO 2080210 | -3.0 | 12.13 | 15.42 | 9.95 | 1.141 | 8.250 | 15.87 | 0.03163 | 39.88 | 0.195 |
| ESO 3060170 | -4.0 | 13.17 | 210.90 | 11.56 | 0.353 | 18.000 | 631.51 | 1.06222 | 43.60 | 0.017 |
| ESO 3220600 | -2.2 | 13.36 | 45.85 | 10.36 | 0.887 | 1.226 | 9.26 | 0.02710 | < 40.72 | |
| ESO 3510300 | 0.0 | 9.72 | 2.34 | 9.02 | 0.185 | 4.650 | 11.65 | 0.03290 | < 38.16 | |
| ESO 3560040 | -5.0 | 8.55 | 0.94 | 8.70 | 0.242 | 11.250 | 16.09 | 0.04240 | < 37.48 | |
| ESO 4000300 | | 13.47 | 45.25 | 10.12 | 0.420 | 0.497 | 9.03 | 0.02473 | < 40.63 | |
| ESO 4250190 | -3.0 | 13.38 | 130.14 | 11.09 | 0.425 | 12.000 | 28.32 | 0.04065 | 41.78 | 0.124 |
| ESO 4280110 | -3.0 | 14.53 | 15.74 | 9.23 | 2.217 | 1.214 | 9.25 | 0.02258 | < 39.78 | |
| ESO 5070210 | -3.0 | 13.18 | 61.00 | 10.59 | 0.667 | 15.500 | 11.25 | 0.03871 | 41.13 | 0.169 |
| ESO 5520200 | -4.0 | 13.18 | 186.75 | 11.48 | 0.425 | 16.000 | 93.69 | 0.22298 | 42.84 | 0.120 |
| ESO 5530020 | -2.3 | 13.32 | 93.94 | 10.83 | 0.500 | 12.250 | 28.11 | 0.06659 | 41.72 | 0.136 |
| ESO 5650300 | -3.0 | 13.49 | 141.30 | 11.12 | 0.403 | 10.500 | 51.02 | 0.11409 | 42.30 | 0.126 |
| ESO 920130 | -4.0 | 12.96 | 29.67 | 10.83 | 1.731 | 2.197 | 9.70 | 0.03273 | < 40.46 | |
| E 273-G002 | 0.0 | 14.08 | 4.80 | 8.17 | 1.063 | 1.014 | 9.22 | 0.02683 | < 38.76 | |
| E 286-G050 | -3.0 | 13.51 | 51.20 | 10.20 | 0.361 | 0.883 | 9.11 | 0.02559 | < 40.73 | |
| E 381-G029 | 0.0 | 13.63 | 46.52 | 10.13 | 0.444 | 0.243 | 9.01 | 0.02898 | < 40.73 | |
| IC 310 | -2.0 | 13.72 | 111.24 | 11.01 | 1.190 | 15.000 | 325.43 | 0.65455 | 42.91 | 0.034 |
| IC 1459 | -5.0 | 10.92 | 33.11 | 10.85 | 0.115 | 11.750 | 31.32 | 0.14620 | 41.06 | 0.094 |
| IC 1531 | -3.0 | 13.34 | 154.12 | 11.21 | 0.156 | 12.500 | 12.40 | 0.03431 | 41.83 | 0.160 |
| IC 1625 | -3.3 | 12.78 | 132.89 | 11.31 | 0.229 | 12.750 | 17.98 | 0.06631 | 41.99 | 0.164 |
| IC 1633 | -4.0 | 12.86 | 143.91 | 11.35 | 0.210 | 23.750 | 78.42 | 0.25184 | 42.64 | 0.136 |
| IC 1729 | -4.0 | 13.38 | 30.14 | 9.77 | 0.142 | 0.395 | 9.02 | 0.02489 | < 40.26 | |
| IC 1860 | -5.0 | 13.26 | 138.30 | 11.15 | 0.227 | 15.000 | 253.07 | 0.58530 | 42.97 | 0.026 |
| IC 2006 | -4.5 | 12.17 | 26.13 | 10.13 | 0.118 | 1.432 | 9.01 | 0.31844 | < 41.19 | |
| IC 2035 | -2.0 | 12.47 | 17.99 | 9.69 | 0.214 | 0.255 | 9.00 | 0.12719 | < 40.52 | |
| IC 2311 | -5.0 | 13.54 | 31.94 | 10.34 | 1.536 | 0.883 | 9.13 | 0.02273 | < 40.36 | |
| IC 2533 | -3.0 | 12.90 | 47.18 | 10.45 | 0.583 | 0.647 | 9.09 | 0.02217 | < 40.62 | |
| IC 2552 | -3.0 | 13.35 | 51.68 | 10.43 | 0.815 | 1.839 | 9.49 | 0.02529 | < 40.78 | |
| IC 2597 | -4.0 | 12.76 | 52.68 | 10.61 | 0.497 | 1.047 | 9.33 | 0.02530 | < 40.78 | |
| IC 3896 | | 12.16 | 39.66 | 10.90 | 1.742 | 2.119 | 9.50 | 0.03301 | < 40.72 | |
| IC 4197 | -3.0 | 13.48 | 55.34 | 10.38 | 0.928 | 0.859 | 9.09 | 0.02569 | < 40.88 | |
| IC 4296 | -5.0 | 11.42 | 69.17 | 11.33 | 0.409 | 17.250 | 22.34 | 0.07249 | 41.49 | 0.143 |
| IC 4765 | -4.0 | 12.26 | 90.16 | 11.29 | 0.604 | 9.500 | 31.05 | 0.19862 | 42.16 | 0.117 |
| IC 4797 | -4.3 | 12.35 | 50.22 | 10.75 | 0.697 | 0.883 | 9.08 | 0.06779 | < 41.19 | |
| IC 4889 | -5.0 | 12.01 | 44.07 | 10.72 | 0.524 | 1.164 | 9.12 | 0.05782 | < 40.98 | |
| IC 4943 | -5.0 | 13.50 | 55.70 | 10.32 | 0.509 | 0.904 | 9.22 | 0.02852 | < 40.88 | |
| IC 5181 | -2.0 | 12.49 | 39.84 | 10.37 | 0.241 | 0.453 | 9.03 | 0.02574 | < 40.52 | |
| IC 5358 | -4.0 | 13.37 | 174.32 | 11.31 | 0.155 | 23.000 | 1126.61 | 2.94624 | 43.87 | 0.013 |
| Leo I | -5.0 | 11.18 | 0.75 | 7.59 | 0.369 | 7.451 | 19.34 | 0.04407 | < 37.30 | |
| Leo II | -5.0 | 12.60 | 0.13 | 5.41 | 0.121 | 8.235 | 17.69 | 0.06165 | < 35.83 | |
| MaffI | -3.0 | 11.40 | 5.30 | 9.05 | 7.788 | 1.500 | 9.73 | 0.01578 | < 38.76 | |
| NGC 57 | -5.0 | 12.67 | 113.64 | 11.22 | 0.400 | 8.750 | 30.48 | 0.12203 | 42.14 | 0.082 |
| NGC 147 | -5.0 | 10.47 | 2.72 | 9.15 | 1.264 | 7.444 | 22.03 | 0.03895 | < 38.44 | |
| NGC 185 | -5.0 | 10.10 | 0.87 | 8.33 | 1.325 | 5.686 | 17.31 | 0.03371 | < 37.39 | |
| NGC 205 | -5.0 | 8.71 | 6.46 | 10.36 | 0.732 | 7.976 | 24.50 | 0.04707 | < 39.25 | |
| NGC 221 | -6.0 | 9.07 | 6.43 | 10.28 | 0.627 | 13.750 | 86.64 | 0.16823 | 39.81 | 0.056 |
| NGC 315 | -4.0 | 11.79 | 107.15 | 11.61 | 0.593 | 10.000 | 31.64 | 0.06685 | 41.83 | 0.098 |
| NGC 404 | -3.0 | 10.16 | 6.09 | 9.76 | 0.509 | 1.400 | 9.94 | 0.02067 | < 38.81 | |
| NGC 410 | -4.0 | 12.42 | 103.05 | 11.30 | 0.588 | 13.750 | 100.36 | 0.21285 | 42.30 | 0.048 |
| NGC 439 | -3.3 | 12.29 | 116.14 | 11.39 | 0.240 | 14.750 | 26.90 | 0.08020 | 41.96 | 0.103 |
| NGC 499 | -2.5 | 12.99 | 100.39 | 11.04 | 0.525 | 15.000 | 163.03 | 0.42966 | 42.58 | 0.045 |
| NGC 507 | -2.0 | 11.80 | 100.37 | 11.52 | 0.525 | 25.000 | 419.00 | 1.10762 | 42.99 | 0.035 |
| NGC 533 | -5.0 | 12.32 | 113.07 | 11.37 | 0.308 | 16.250 | 207.79 | 0.47658 | 42.71 | 0.052 |
| NGC 568 | -3.0 | 13.43 | 112.04 | 10.90 | 0.197 | 8.500 | 18.34 | 0.04937 | 41.71 | 0.128 |
| NGC 584 | -5.0 | 11.40 | 39.62 | 10.86 | 0.330 | 1.368 | 9.21 | 0.02057 | < 40.41 | |

**Table 1 –** *continued*

| Name | $T$ RC3 | $B_T$ mag | $D$ Mpc | $\log(L_B)$ $L_\odot$ | $n_H$ $10^{-21}$ cm$^{-2}$ | $R$ arcmin | Counts | Count rate s$^{-1}$ | $\log(L_x)$ erg s$^{-1}$ | Error dex |
|---|---|---|---|---|---|---|---|---|---|---|
| NGC 596 | -4.0 | 11.77 | 39.59 | 10.70 | 0.330 | 1.500 | 9.23 | 0.02066 | < 40.43 | |
| NGC 636 | -5.0 | 12.46 | 39.48 | 10.42 | 0.307 | 0.946 | 9.11 | 0.02011 | < 40.42 | |
| NGC 708 | -5.0 | 12.34 | 99.71 | 11.32 | 0.552 | 40.000 | 1088.08 | 3.15622 | 43.44 | 0.016 |
| NGC 720 | -5.0 | 11.16 | 35.20 | 10.79 | 0.169 | 25.500 | 91.86 | 0.19348 | 41.30 | 0.056 |
| NGC 741 | -5.0 | 12.19 | 108.32 | 11.41 | 0.427 | 13.750 | 53.93 | 0.12566 | 42.12 | 0.067 |
| NGC 777 | -5.0 | 12.52 | 99.42 | 11.21 | 0.546 | 12.500 | 101.65 | 0.32607 | 42.46 | 0.047 |
| NGC 821 | -5.0 | 11.73 | 37.69 | 10.69 | 0.616 | 2.428 | 10.23 | 0.03828 | < 40.66 | |
| NGC 855 | -5.0 | 13.33 | 16.41 | 9.35 | 0.633 | 0.879 | 9.26 | 0.04852 | < 40.07 | |
| NGC 1052 | -5.0 | 11.34 | 29.30 | 10.59 | 0.299 | 1.845 | 9.26 | 0.04004 | < 40.46 | |
| NGC 1172 | -3.7 | 12.66 | 47.08 | 10.49 | 0.423 | 1.932 | 9.33 | 0.03731 | < 40.85 | |
| NGC 1199 | -5.0 | 12.34 | 46.98 | 10.61 | 0.424 | 1.466 | 9.19 | 0.03444 | < 40.81 | |
| NGC 1201 | -2.0 | 11.64 | 32.96 | 10.54 | 0.155 | 1.355 | 9.18 | 0.03331 | < 40.48 | |
| NGC 1209 | -5.0 | 12.41 | 46.95 | 10.58 | 0.423 | 0.883 | 9.08 | 0.04086 | < 40.88 | |
| NGC 1316 | | 9.40 | 26.43 | 11.25 | 0.241 | 17.000 | 62.27 | 0.24482 | 41.15 | 0.136 |
| NGC 1336 | -3.3 | 13.08 | 25.08 | 9.73 | 0.200 | 1.514 | 9.18 | 0.04878 | < 40.39 | |
| NGC 1339 | -4.4 | 12.51 | 26.78 | 10.02 | 0.124 | 0.844 | 9.05 | 0.04753 | < 40.37 | |
| NGC 1340 | | 11.20 | 23.98 | 10.44 | 0.115 | 1.642 | 9.16 | 0.05423 | < 40.33 | |
| NGC 1351 | | 12.30 | 26.53 | 10.09 | 0.135 | 1.277 | 9.13 | 0.05180 | < 40.48 | |
| NGC 1366 | -2.0 | 12.85 | 25.08 | 9.82 | 0.109 | 0.493 | 9.01 | 0.06054 | < 40.42 | |
| NGC 1374 | -4.5 | 11.88 | 26.44 | 10.26 | 0.139 | 1.500 | 9.28 | 0.05096 | < 40.47 | |
| NGC 1375 | -2.0 | 13.12 | 15.78 | 9.31 | 0.139 | 0.739 | 9.07 | 0.04944 | < 39.99 | |
| NGC 1379 | -5.0 | 11.66 | 26.41 | 10.34 | 0.139 | 2.119 | 9.71 | 0.05547 | < 40.49 | |
| NGC 1380 | | 10.94 | 33.78 | 10.84 | 0.145 | 2.027 | 9.57 | 0.05321 | < 40.69 | |
| NGC 1395 | -5.0 | 10.96 | 30.90 | 10.77 | 0.184 | 25.500 | 28.66 | 0.20644 | 41.22 | 0.111 |
| NGC 1399 | -5.0 | 10.55 | 26.38 | 10.79 | 0.145 | 35.000 | 482.99 | 2.58200 | 42.18 | 0.040 |
| NGC 1400 | -3.0 | 11.76 | 31.26 | 10.51 | 0.479 | 1.888 | 9.42 | 0.02738 | < 40.37 | |
| NGC 1404 | -5.0 | 10.89 | 26.36 | 10.65 | 0.145 | 27.750 | 66.91 | 0.34044 | 41.30 | 0.129 |
| NGC 1407 | -5.0 | 10.74 | 31.26 | 10.93 | 0.525 | 19.000 | 51.90 | 0.15846 | 41.14 | 0.092 |
| NGC 1411 | -3.0 | 12.07 | 19.12 | 9.90 | 0.190 | 0.677 | 9.04 | 0.03010 | < 39.95 | |
| NGC 1419 | -5.4 | 13.41 | 26.19 | 9.64 | 0.204 | 0.545 | 9.02 | 0.05923 | < 40.51 | |
| NGC 1426 | -5.0 | 12.27 | 30.92 | 10.24 | 0.230 | 1.306 | 9.25 | 0.01949 | < 40.17 | |
| NGC 1427 | | 11.76 | 26.33 | 10.30 | 0.109 | 1.645 | 9.29 | 0.07123 | < 40.53 | |
| NGC 1439 | -5.0 | 12.14 | 30.91 | 10.32 | 0.232 | 2.071 | 9.64 | 0.01879 | < 40.16 | |
| NGC 1537 | -2.5 | 11.53 | 22.71 | 10.26 | 0.243 | 1.306 | 9.28 | 0.01645 | < 39.83 | |
| NGC 1549 | -5.0 | 10.58 | 19.57 | 10.52 | 0.153 | 2.377 | 10.23 | 0.01963 | < 39.80 | |
| NGC 1550 | -3.2 | 13.07 | 72.58 | 10.83 | 1.159 | 26.250 | 588.75 | 2.08495 | 43.04 | 0.029 |
| NGC 1553 | -2.0 | 10.26 | 18.20 | 10.58 | 0.153 | 16.500 | 44.93 | 0.08286 | 40.36 | 0.085 |
| NGC 1573 | -5.0 | 12.77 | 88.61 | 11.13 | 0.937 | 8.500 | 21.33 | 0.05846 | 41.65 | 0.111 |
| NGC 1581 | -3.0 | 13.50 | 25.84 | 9.59 | 0.155 | 0.482 | 9.03 | 0.02743 | < 40.17 | |
| NGC 1600 | -5.0 | 11.87 | 98.59 | 11.44 | 0.517 | 14.250 | 27.74 | 0.07793 | 41.83 | 0.113 |
| NGC 1705 | -3.0 | 12.77 | 9.54 | 9.09 | 0.350 | 0.577 | 9.11 | 0.01060 | < 38.89 | |
| NGC 2089 | -3.0 | 12.95 | 57.10 | 10.62 | 0.659 | 1.074 | 9.20 | 0.01861 | < 40.74 | |
| NGC 2271 | -3.0 | 13.12 | 48.20 | 10.69 | 1.454 | 1.582 | 9.26 | 0.02908 | < 40.84 | |
| NGC 2272 | -3.0 | 12.78 | 1.07 | 7.40 | 1.056 | 1.194 | 9.16 | 0.02583 | < 37.44 | |
| NGC 2292 | -2.0 | 11.81 | 36.46 | 11.05 | 1.510 | 9.685 | 17.45 | 0.03460 | < 40.65 | |
| NGC 2293 | -1.0 | 13.02 | 36.46 | 10.56 | 1.510 | 1.466 | 9.38 | 0.01865 | < 40.39 | |
| NGC 2300 | -2.0 | 11.95 | 45.58 | 10.79 | 0.528 | 14.000 | 148.10 | 0.19470 | 41.55 | 0.099 |
| NGC 2305 | -5.0 | 12.55 | 66.24 | 10.91 | 0.653 | 26.500 | 425.72 | 0.17144 | 41.85 | 0.025 |
| NGC 2325 | -5.0 | 12.31 | 40.83 | 10.94 | 1.564 | 14.250 | 16.70 | 0.03828 | 40.81 | 0.135 |
| NGC 2328 | -2.9 | 13.01 | 18.40 | 9.68 | 0.940 | 0.567 | 9.06 | 0.01602 | < 39.72 | |
| NGC 2329 | -3.0 | 13.37 | 117.31 | 11.09 | 0.697 | 14.000 | 73.61 | 0.20651 | 42.43 | 0.056 |
| NGC 2340 | -5.0 | 12.45 | 117.42 | 11.44 | 0.710 | 13.250 | 64.45 | 0.17614 | 42.36 | 0.076 |
| NGC 2380 | -1.7 | 13.18 | 31.18 | 10.67 | 3.488 | 2.168 | 9.60 | 0.02105 | < 40.36 | |
| NGC 2434 | -5.0 | 12.19 | 21.40 | 10.25 | 1.258 | 9.250 | 16.31 | 0.02565 | 40.07 | 0.137 |
| NGC 2488 | -3.0 | 13.40 | 174.47 | 11.23 | 0.419 | 15.000 | 100.56 | 0.22968 | 42.79 | 0.083 |
| NGC 2502 | -2.0 | 13.14 | 16.38 | 9.74 | 2.396 | 0.882 | 9.17 | 0.01095 | < 39.49 | |
| NGC 2563 | -2.0 | 12.98 | 95.21 | 10.99 | 0.416 | 15.000 | 50.88 | 0.17685 | 42.15 | 0.110 |
| NGC 2577 | -3.0 | 13.40 | 41.97 | 10.10 | 0.367 | 0.672 | 9.07 | 0.03572 | < 40.70 | |
| NGC 2634 | | 12.84 | 46.69 | 10.38 | 0.213 | 1.247 | 9.62 | 0.02108 | < 40.57 | |
| NGC 2663 | -4.6 | 12.05 | 35.57 | 11.08 | 2.862 | 13.000 | 10.77 | 0.02207 | 40.50 | 0.200 |
| NGC 2695 | -2.0 | 12.80 | 32.93 | 10.10 | 0.243 | 0.824 | 9.07 | 0.02677 | < 40.37 | |
| NGC 2768 | -5.0 | 11.09 | 27.69 | 10.68 | 0.383 | 3.054 | 11.27 | 0.02131 | < 40.14 | |
| NGC 2778 | -5.0 | 13.32 | 37.20 | 9.99 | 0.200 | 0.778 | 9.30 | 0.02048 | < 40.36 | |
| NGC 2832 | -4.0 | 12.80 | 136.21 | 11.31 | 0.165 | 13.750 | 100.57 | 0.22561 | 42.54 | 0.105 |

**Table 1 –** *continued*

| Name | $T$ RC3 | $B_T$ mag | $D$ Mpc | $\log(L_B)$ $L_\odot$ | $n_H$ $10^{-21}$ cm$^{-2}$ | $R$ arcmin | Counts | Count rate s$^{-1}$ | $\log(L_x)$ erg s$^{-1}$ | Error dex |
|---|---|---|---|---|---|---|---|---|---|---|
| NGC 2865 | -5.0 | 12.58 | 44.15 | 10.54 | 0.613 | 0.584 | 9.07 | 0.01834 | < 40.48 | |
| NGC 2880 | -3.0 | 12.46 | 33.69 | 10.25 | 0.308 | 1.052 | 9.35 | 0.01660 | < 40.18 | |
| NGC 2887 | -3.0 | 12.59 | 51.09 | 10.89 | 1.853 | 1.368 | 9.26 | 0.02722 | < 40.85 | |
| NGC 2888 | -4.0 | 13.47 | 43.89 | 10.26 | 0.773 | 0.735 | 9.08 | 0.01716 | < 40.47 | |
| NGC 2904 | -3.0 | 13.88 | 42.21 | 10.15 | 1.068 | 0.735 | 9.08 | 0.01956 | < 40.51 | |
| NGC 2974 | -5.0 | 11.57 | 36.36 | 10.71 | 0.382 | 1.845 | 9.38 | 0.02047 | < 40.38 | |
| NGC 2986 | -5.0 | 11.61 | 38.61 | 10.73 | 0.441 | 12.250 | 36.84 | 0.07724 | 41.01 | 0.105 |
| NGC 3073 | -2.5 | 14.07 | 25.44 | 9.43 | 0.078 | 0.508 | 9.18 | 0.01575 | < 39.85 | |
| NGC 3078 | -5.0 | 12.11 | 45.20 | 10.70 | 0.406 | 10.250 | 15.00 | 0.03653 | 40.82 | 0.164 |
| NGC 3087 | -4.2 | 12.96 | 50.21 | 10.63 | 0.955 | 0.806 | 9.12 | 0.02192 | < 40.71 | |
| NGC 3091 | -5.0 | 12.24 | 67.12 | 10.98 | 0.449 | 12.250 | 34.97 | 0.06862 | 41.44 | 0.089 |
| NGC 3115 | -3.0 | 10.05 | 9.62 | 10.15 | 0.448 | 1.803 | 9.38 | 0.02009 | < 39.22 | |
| NGC 3136 | | 11.23 | 28.26 | 10.57 | 1.731 | 2.071 | 9.61 | 0.03280 | < 40.42 | |
| NGC 3156 | -2.0 | 12.05 | 22.80 | 10.08 | 0.223 | 0.693 | 9.18 | 0.02051 | < 39.93 | |
| NGC 3158 | -5.0 | 12.92 | 136.46 | 11.28 | 0.135 | 11.500 | 29.42 | 0.06024 | 41.97 | 0.132 |
| NGC 3193 | -5.0 | 11.89 | 23.88 | 10.20 | 0.204 | 1.335 | 9.90 | 0.02202 | < 40.00 | |
| NGC 3224 | -4.0 | 13.09 | 51.68 | 10.57 | 0.831 | 0.879 | 9.13 | 0.02275 | < 40.74 | |
| NGC 3226 | -5.0 | 11.95 | 23.67 | 10.14 | 0.222 | 12.500 | 42.59 | 0.08862 | 40.62 | 0.088 |
| NGC 3250 | | 12.20 | 53.84 | 10.96 | 0.726 | 1.607 | 9.50 | 0.02262 | < 40.79 | |
| NGC 3375 | -2.0 | 13.34 | 42.71 | 10.11 | 0.351 | 1.038 | 9.15 | 0.02327 | < 40.53 | |
| NGC 3377 | | 11.19 | 13.33 | 9.96 | 0.285 | 1.662 | 9.79 | 0.03149 | < 39.65 | |
| NGC 3379 | -5.0 | 10.48 | 13.19 | 10.23 | 0.285 | 1.760 | 9.76 | 0.02732 | < 39.58 | |
| NGC 3384 | -3.0 | 10.85 | 12.05 | 10.03 | 0.265 | 1.161 | 9.40 | 0.02616 | < 39.48 | |
| NGC 3557 | | 11.68 | 52.70 | 11.16 | 0.832 | 1.888 | 9.61 | 0.02625 | < 40.82 | |
| NGC 3585 | -5.0 | 10.83 | 24.25 | 10.72 | 0.561 | 1.977 | 9.45 | 0.02783 | < 40.16 | |
| NGC 3599 | -2.0 | 12.69 | 20.44 | 9.71 | 0.139 | 1.184 | 9.54 | 0.02585 | < 39.94 | |
| NGC 3606 | -5.0 | 13.83 | 55.15 | 10.25 | 0.666 | 0.597 | 9.05 | 0.02559 | < 40.85 | |
| NGC 3610 | -5.0 | 11.72 | 39.08 | 10.66 | 0.085 | 0.767 | 9.29 | 0.01583 | < 40.22 | |
| NGC 3613 | -5.0 | 11.85 | 39.00 | 10.61 | 0.073 | 1.284 | 9.81 | 0.01709 | < 40.25 | |
| NGC 3617 | -4.0 | 13.60 | 24.29 | 9.60 | 0.563 | 0.597 | 9.05 | 0.02640 | < 40.12 | |
| NGC 3640 | -5.0 | 11.34 | 27.07 | 10.53 | 0.443 | 1.597 | 10.03 | 0.02290 | < 40.15 | |
| NGC 3656 | 90.0 | 12.86 | 59.80 | 10.57 | 0.106 | 1.100 | 9.47 | 0.02358 | < 40.77 | |
| NGC 3706 | -3.0 | 12.21 | 49.48 | 10.82 | 0.658 | 1.277 | 9.08 | 0.08696 | < 41.28 | |
| NGC 3818 | -5.0 | 12.68 | 25.75 | 9.96 | 0.321 | 1.062 | 9.14 | 0.02510 | < 40.13 | |
| NGC 3862 | -5.0 | 13.48 | 124.70 | 10.96 | 0.255 | 10.000 | 46.67 | 0.10268 | 42.13 | 0.155 |
| NGC 3904 | -5.0 | 11.86 | 31.55 | 10.49 | 0.627 | 1.164 | 9.04 | 0.12939 | < 41.07 | |
| NGC 3923 | -5.0 | 10.77 | 31.58 | 10.95 | 0.627 | 2.667 | 9.20 | 0.16922 | < 41.20 | |
| NGC 3962 | -5.0 | 11.63 | 32.52 | 10.55 | 0.394 | 1.758 | 9.26 | 0.02714 | < 40.39 | |
| NGC 4024 | -3.0 | 12.54 | 28.29 | 10.08 | 0.350 | 1.277 | 9.22 | 0.02059 | < 40.12 | |
| NGC 4033 | -5.0 | 12.59 | 28.33 | 10.06 | 0.380 | 0.806 | 9.09 | 0.02057 | < 40.15 | |
| NGC 4036 | -3.0 | 11.57 | 30.52 | 10.54 | 0.192 | 1.390 | 9.83 | 0.01869 | < 40.14 | |
| NGC 4073 | -3.8 | 12.24 | 115.25 | 11.40 | 0.186 | 36.250 | 515.64 | 1.30798 | 43.16 | 0.034 |
| NGC 4105 | -5.0 | 11.46 | 34.86 | 10.76 | 0.498 | 2.071 | 9.22 | 0.06483 | < 40.83 | |
| NGC 4125 | -5.0 | 10.61 | 38.26 | 11.10 | 0.185 | 15.000 | 65.99 | 0.10637 | 41.11 | 0.076 |
| NGC 4168 | -5.0 | 12.00 | 43.77 | 10.67 | 0.249 | 1.427 | 9.88 | 0.02228 | < 40.53 | |
| NGC 4203 | -3.0 | 11.80 | 21.40 | 10.18 | 0.120 | 17.500 | 287.33 | 0.56175 | 41.27 | 0.039 |
| NGC 4239 | -5.0 | 13.66 | 21.05 | 9.38 | 0.258 | 0.756 | 9.24 | 0.02049 | < 39.86 | |
| NGC 4261 | -5.0 | 11.32 | 40.98 | 10.86 | 0.163 | 10.750 | 60.41 | 0.13986 | 41.29 | 0.091 |
| NGC 4262 | -3.0 | 12.49 | 25.20 | 10.04 | 0.243 | 0.654 | 9.23 | 0.02115 | < 40.03 | |
| NGC 4267 | -3.0 | 11.86 | 17.64 | 9.95 | 0.269 | 2.069 | 11.06 | 0.02551 | < 39.80 | |
| NGC 4278 | -5.0 | 11.12 | 14.56 | 10.08 | 0.172 | 7.500 | 22.77 | 0.04618 | 39.91 | 0.109 |
| NGC 4283 | -5.0 | 13.10 | 14.57 | 9.29 | 0.172 | 0.625 | 9.19 | 0.01864 | < 39.50 | |
| NGC 4291 | -5.0 | 12.48 | 36.67 | 10.32 | 0.280 | 7.500 | 80.77 | 0.11756 | 41.12 | 0.087 |
| NGC 4339 | -5.0 | 12.29 | 20.09 | 9.85 | 0.163 | 1.607 | 9.97 | 0.02294 | < 39.87 | |
| NGC 4365 | -5.0 | 10.64 | 20.21 | 10.52 | 0.162 | 7.500 | 17.59 | 0.04008 | 40.14 | 0.148 |
| NGC 4374 | -5.0 | 10.26 | 20.74 | 10.75 | 0.263 | 16.000 | 60.90 | 0.13545 | 40.69 | 0.090 |
| NGC 4406 | -5.0 | 9.98 | 20.75 | 10.85 | 0.264 | 59.250 | 1247.30 | 2.78291 | 42.00 | 0.002 |
| NGC 4434 | -5.0 | 12.83 | 20.31 | 9.65 | 0.159 | 0.769 | 9.44 | 0.02142 | < 39.85 | |
| NGC 4458 | -5.0 | 12.86 | 20.80 | 9.69 | 0.259 | 1.305 | 11.74 | 0.02639 | < 39.96 | |
| NGC 4464 | 0.0 | 13.61 | 20.32 | 9.34 | 0.159 | 0.149 | 9.02 | 0.02060 | < 39.83 | |
| NGC 4472 | -5.0 | 9.32 | 20.31 | 11.05 | 0.159 | 33.750 | 648.29 | 1.49440 | 41.71 | 0.043 |
| NGC 4473 | -5.0 | 11.25 | 20.82 | 10.32 | 0.259 | 1.257 | 11.26 | 0.02536 | < 39.95 | |
| NGC 4486 | | 9.61 | 20.73 | 10.99 | 0.250 | 63.500 | 14714.80 | 33.1394 | 43.08 | 0.007 |
| NGC 4489 | -5.0 | 12.74 | 21.15 | 9.73 | 0.237 | 1.398 | 9.88 | 0.02186 | < 39.89 | |

**Table 1 –** *continued*

| Name | $T$ RC3 | $B_T$ mag | $D$ Mpc | $\log(L_B)$ $L_\odot$ | $n_H$ $10^{-21}$ cm$^{-2}$ | $R$ arcmin | Counts | Count rate s$^{-1}$ | $\log(L_x)$ erg s$^{-1}$ | Error dex |
|---|---|---|---|---|---|---|---|---|---|---|
| NGC 4494 | -5.0 | 10.75 | 22.45 | 10.59 | 0.154 | 2.407 | 10.98 | 0.02255 | < 39.96 | |
| NGC 4503 | -3.0 | 12.05 | 24.84 | 10.13 | 0.212 | 1.166 | 10.64 | 0.02393 | < 40.07 | |
| NGC 4515 | -3.0 | 13.30 | 16.86 | 9.29 | 0.229 | 0.557 | 9.18 | 0.02028 | < 39.66 | |
| NGC 4551 | -5.0 | 12.84 | 20.75 | 9.71 | 0.259 | 0.651 | 9.51 | 0.02123 | < 39.86 | |
| NGC 4552 | -5.0 | 10.98 | 20.78 | 10.46 | 0.259 | 12.500 | 57.79 | 0.12883 | 40.67 | 0.085 |
| NGC 4564 | -5.0 | 12.00 | 20.68 | 10.01 | 0.250 | 0.906 | 9.76 | 0.02193 | < 39.88 | |
| NGC 4581 | -4.0 | 13.17 | 33.08 | 9.94 | 0.178 | 0.768 | 9.20 | 0.02962 | < 40.41 | |
| NGC 4589 | -5.0 | 11.63 | 36.61 | 10.66 | 0.197 | 1.923 | 11.81 | 0.01310 | < 40.15 | |
| NGC 4621 | -5.0 | 10.72 | 20.74 | 10.54 | 0.201 | 1.992 | 11.06 | 0.02461 | < 39.93 | |
| NGC 4627 | -5.0 | 11.62 | 14.15 | 9.83 | 0.123 | 11.750 | 26.04 | 0.04983 | 39.86 | 0.121 |
| NGC 4636 | -5.0 | 10.21 | 19.92 | 10.68 | 0.175 | 20.000 | 236.01 | 1.45848 | 41.68 | 0.046 |
| NGC 4638 | -3.0 | 12.13 | 20.30 | 9.96 | 0.201 | 0.859 | 9.47 | 0.02106 | < 39.84 | |
| NGC 4645 | | 12.73 | 55.08 | 10.75 | 0.887 | 1.087 | 9.23 | 0.02613 | < 40.87 | |
| NGC 4648 | -5.0 | 12.80 | 36.63 | 10.20 | 0.197 | 0.657 | 9.44 | 0.01041 | < 40.05 | |
| NGC 4649 | -5.0 | 9.81 | 20.74 | 10.89 | 0.194 | 19.000 | 233.84 | 0.51944 | 41.27 | 0.042 |
| NGC 4660 | -5.0 | 12.19 | 20.71 | 9.92 | 0.194 | 0.605 | 9.24 | 0.02053 | < 39.85 | |
| NGC 4696 | | 10.44 | 55.12 | 11.65 | 0.825 | 52.000 | 2869.38 | 8.39688 | 43.38 | 0.008 |
| NGC 4697 | -5.0 | 10.07 | 22.48 | 10.86 | 0.212 | 20.250 | 24.11 | 0.06998 | 40.47 | 0.137 |
| NGC 4733 | -4.0 | 12.70 | 16.04 | 9.43 | 0.200 | 1.285 | 9.98 | 0.01689 | < 39.54 | |
| NGC 4742 | -5.0 | 12.13 | 23.02 | 10.08 | 0.347 | 0.584 | 9.05 | 0.03279 | < 40.14 | |
| NGC 4751 | -3.0 | 12.95 | 35.30 | 10.24 | 0.702 | 1.020 | 9.16 | 0.02608 | < 40.47 | |
| NGC 4754 | -3.0 | 11.52 | 25.65 | 10.45 | 0.201 | 1.220 | 9.88 | 0.01673 | < 39.95 | |
| NGC 4760 | -5.0 | 12.33 | 88.24 | 11.16 | 0.342 | 23.250 | 25.99 | 0.08237 | 41.73 | 0.105 |
| NGC 4767 | | 12.34 | 55.19 | 10.87 | 0.786 | 1.535 | 9.33 | 0.02744 | < 40.88 | |
| NGC 4915 | -5.0 | 13.06 | 59.45 | 10.50 | 0.212 | 0.395 | 9.02 | 0.03309 | < 40.97 | |
| NGC 4936 | -5.0 | 11.58 | 60.17 | 11.23 | 0.619 | 16.750 | 75.65 | 0.23792 | 41.88 | 0.096 |
| NGC 4946 | -4.0 | 13.36 | 59.37 | 10.54 | 0.889 | 0.844 | 9.09 | 0.03043 | < 41.00 | |
| NGC 4976 | -5.0 | 11.72 | 22.96 | 10.58 | 1.472 | 2.023 | 9.56 | 0.02691 | < 40.14 | |
| NGC 4993 | -2.6 | 13.28 | 54.90 | 10.45 | 0.898 | 0.830 | 9.09 | 0.02626 | < 40.87 | |
| NGC 5011 | | 12.36 | 59.43 | 10.93 | 0.741 | 1.248 | 9.25 | 0.03237 | < 41.03 | |
| NGC 5018 | -5.0 | 11.63 | 50.11 | 11.00 | 0.726 | 1.248 | 9.20 | 0.02652 | < 40.80 | |
| NGC 5044 | -5.0 | 11.37 | 50.33 | 11.07 | 0.491 | 33.750 | 1135.50 | 3.96426 | 42.95 | 0.031 |
| NGC 5061 | -5.0 | 11.33 | 32.50 | 10.76 | 0.636 | 1.277 | 9.22 | 0.03067 | < 40.48 | |
| NGC 5077 | -5.0 | 12.28 | 50.63 | 10.69 | 0.299 | 1.248 | 9.16 | 0.03719 | < 40.90 | |
| NGC 5087 | -3.0 | 12.14 | 32.87 | 10.47 | 0.775 | 18.000 | 14.89 | 0.04630 | 40.67 | 0.144 |
| NGC 5090 | | 12.51 | 71.02 | 11.05 | 0.851 | 12.250 | 38.83 | 0.13399 | 41.80 | 0.110 |
| NGC 5102 | -3.0 | 10.79 | 3.32 | 8.98 | 0.426 | 1.306 | 9.39 | 0.03250 | < 38.48 | |
| NGC 5129 | -5.0 | 12.93 | 140.25 | 11.30 | 0.175 | 10.750 | 49.29 | 0.13616 | 42.35 | 0.103 |
| NGC 5173 | -5.0 | 13.10 | 49.58 | 10.30 | 0.180 | 0.486 | 9.11 | 0.01521 | < 40.48 | |
| NGC 5198 | -5.0 | 12.61 | 51.28 | 10.54 | 0.180 | 1.273 | 9.83 | 0.01619 | < 40.53 | |
| NGC 5216 | -5.0 | 13.58 | 62.38 | 10.33 | 0.185 | 10.375 | 19.80 | 0.03223 | 41.02 | 0.198 |
| NGC 5253 | 10.0 | 10.67 | 3.36 | 9.03 | 0.390 | 1.025 | 9.13 | 0.03132 | < 38.48 | |
| NGC 5308 | -3.0 | 12.31 | 43.73 | 10.48 | 0.192 | 0.643 | 9.32 | 0.01073 | < 40.22 | |
| NGC 5322 | -5.0 | 11.09 | 42.12 | 10.98 | 0.164 | 1.649 | 10.60 | 0.01457 | < 40.32 | |
| NGC 5328 | -5.0 | 12.65 | 85.49 | 11.07 | 0.443 | 16.250 | 50.11 | 0.16651 | 42.03 | 0.072 |
| NGC 5419 | -4.7 | 11.75 | 85.33 | 11.43 | 0.562 | 12.750 | 32.47 | 0.14692 | 41.98 | 0.092 |
| NGC 5473 | -3.0 | 12.35 | 43.32 | 10.50 | 0.116 | 0.955 | 9.55 | 0.01477 | < 40.28 | |
| NGC 5485 | -2.0 | 12.14 | 38.40 | 10.48 | 0.121 | 1.460 | 10.22 | 0.01567 | < 40.20 | |
| NGC 5546 | -5.0 | 13.30 | 144.77 | 11.15 | 0.213 | 15.000 | 44.60 | 0.09574 | 42.22 | 0.100 |
| NGC 5574 | -3.0 | 13.23 | 30.23 | 9.85 | 0.245 | 0.619 | 9.19 | 0.02377 | < 40.24 | |
| NGC 5576 | -5.0 | 11.79 | 30.35 | 10.43 | 0.245 | 0.882 | 9.33 | 0.02422 | < 40.25 | |
| NGC 5582 | -5.0 | 12.44 | 27.59 | 10.07 | 0.087 | 1.600 | 10.49 | 0.01828 | < 39.98 | |
| NGC 5638 | -5.0 | 12.10 | 30.46 | 10.31 | 0.247 | 1.398 | 9.78 | 0.02775 | < 40.31 | |
| NGC 5687 | -3.0 | 12.60 | 45.09 | 10.40 | 0.121 | 1.427 | 10.34 | 0.01327 | < 40.27 | |
| NGC 5812 | -5.0 | 12.22 | 38.93 | 10.58 | 0.676 | 1.191 | 9.33 | 0.02518 | < 40.54 | |
| NGC 5831 | -5.0 | 12.42 | 31.86 | 10.25 | 0.425 | 1.275 | 10.30 | 0.02627 | < 40.36 | |
| NGC 5838 | -3.0 | 11.92 | 25.73 | 10.30 | 0.425 | 1.003 | 9.91 | 0.02401 | < 40.13 | |
| NGC 5846 | | 10.81 | 31.93 | 10.90 | 0.425 | 23.750 | 317.36 | 0.77000 | 41.84 | 0.050 |
| NGC 5898 | -5.0 | 12.42 | 43.05 | 10.67 | 0.880 | 1.087 | 9.37 | 0.02508 | < 40.64 | |
| NGC 5903 | -5.0 | 12.27 | 43.06 | 10.73 | 0.880 | 1.762 | 9.99 | 0.02668 | < 40.66 | |
| NGC 5982 | -5.0 | 12.00 | 59.31 | 10.92 | 0.187 | 14.000 | 116.90 | 0.08471 | 41.40 | 0.059 |
| NGC 6127 | | 13.00 | 96.01 | 10.96 | 0.161 | 12.500 | 61.27 | 0.05034 | 41.59 | 0.096 |
| NGC 6137 | -5.0 | 13.40 | 188.67 | 11.35 | 0.112 | 22.500 | 95.22 | 0.11252 | 42.46 | 0.131 |
| NGC 6160 | -5.0 | 13.69 | 180.52 | 11.21 | 0.103 | 13.750 | 162.79 | 0.18058 | 42.63 | 0.064 |

**Table 1 –** *continued*

| Name | $T$ RC3 | $B_T$ mag | $D$ Mpc | $\log(L_B)$ $L_\odot$ | $n_H$ $10^{-21}$ cm$^{-2}$ | $R$ arcmin | Counts | Count rate s$^{-1}$ | $\log(L_x)$ erg s$^{-1}$ | Error dex |
|---|---|---|---|---|---|---|---|---|---|---|
| NGC 6166 | -4.0 | 12.76 | 181.93 | 11.58 | 0.084 | 57.750 | 6819.20 | 8.41649 | 44.30 | 0.019 |
| NGC 6173 | -5.0 | 12.93 | 180.54 | 11.51 | 0.103 | 25.000 | 107.67 | 0.12440 | 42.47 | 0.146 |
| NGC 6269 | -5.0 | 13.32 | 201.10 | 11.59 | 0.497 | 45.000 | 266.54 | 0.33035 | 43.07 | 0.038 |
| NGC 6305 | -3.0 | 13.12 | 51.45 | 10.55 | 1.026 | 0.509 | 9.04 | 0.05698 | < 41.15 | |
| NGC 6407 | -2.0 | 12.80 | 89.40 | 11.09 | 0.790 | 15.750 | 34.35 | 0.19797 | 42.17 | 0.089 |
| NGC 6487 | -5.0 | 12.90 | 157.26 | 11.46 | 0.484 | 12.500 | 28.22 | 0.03715 | 41.91 | 0.173 |
| NGC 6673 | -4.0 | 12.59 | 19.08 | 9.83 | 0.778 | 0.707 | 9.06 | 0.05604 | < 40.26 | |
| NGC 6703 | -2.5 | 12.25 | 52.15 | 10.80 | 0.549 | 1.111 | 10.26 | 0.00930 | < 40.33 | |
| NGC 6841 | -4.3 | 13.64 | 0.22 | 5.58 | 0.816 | 0.752 | 9.10 | 0.02936 | < 36.11 | |
| NGC 6851 | | 12.72 | 55.69 | 10.63 | 0.509 | 0.735 | 9.11 | 0.02899 | < 40.88 | |
| NGC 6861 | | 11.92 | 55.71 | 10.94 | 0.509 | 1.138 | 9.36 | 0.02837 | < 40.89 | |
| NGC 6868 | -5.0 | 11.56 | 55.73 | 11.09 | 0.496 | 14.500 | 39.62 | 0.11986 | 41.52 | 0.187 |
| NGC 6909 | -3.8 | 12.48 | 55.98 | 10.70 | 0.433 | 1.535 | 9.36 | 0.04002 | < 41.03 | |
| NGC 6920 | -2.0 | 13.03 | 51.26 | 10.65 | 1.092 | 0.507 | 9.02 | 0.05387 | < 41.14 | |
| NGC 6958 | -3.8 | 12.31 | 52.12 | 10.71 | 0.384 | 1.038 | 9.39 | 0.02986 | < 40.86 | |
| NGC 7007 | -3.0 | 12.87 | 56.69 | 10.54 | 0.374 | 0.746 | 9.12 | 0.03036 | < 40.89 | |
| NGC 7029 | -5.0 | 12.26 | 43.86 | 10.54 | 0.211 | 1.219 | 9.37 | 0.02570 | < 40.60 | |
| NGC 7041 | -2.7 | 12.07 | 43.98 | 10.65 | 0.282 | 1.248 | 9.25 | 0.02499 | < 40.61 | |
| NGC 7049 | -2.0 | 11.60 | 42.94 | 10.80 | 0.282 | 21.000 | 42.39 | 0.11476 | 41.25 | 0.088 |
| NGC 7097 | | 12.48 | 47.62 | 10.53 | 0.262 | 1.087 | 9.13 | 0.03043 | < 40.74 | |
| NGC 7144 | -5.0 | 11.75 | 36.04 | 10.58 | 0.293 | 2.023 | 9.50 | 0.02987 | < 40.49 | |
| NGC 7145 | -5.0 | 11.98 | 36.08 | 10.49 | 0.293 | 1.932 | 9.48 | 0.03063 | < 40.52 | |
| NGC 7166 | -3.0 | 12.74 | 46.86 | 10.41 | 0.188 | 0.520 | 9.03 | 0.02554 | < 40.65 | |
| NGC 7168 | -5.0 | 12.76 | 55.48 | 10.55 | 0.232 | 1.038 | 9.13 | 0.02753 | < 40.83 | |
| NGC 7173 | -4.1 | 12.90 | 52.98 | 10.45 | 0.165 | 0.735 | 9.07 | 0.02897 | < 40.81 | |
| NGC 7176 | -4.6 | 12.34 | 52.97 | 10.72 | 0.165 | 0.015 | 9.00 | 0.02873 | < 40.81 | |
| NGC 7180 | -2.0 | 13.41 | 31.35 | 9.82 | 0.250 | 0.570 | 9.04 | 0.03730 | < 40.47 | |
| NGC 7185 | -3.0 | 13.22 | 31.36 | 9.90 | 0.250 | 1.191 | 9.13 | 0.03422 | < 40.43 | |
| NGC 7192 | -4.3 | 12.04 | 55.66 | 10.84 | 0.227 | 12.750 | 22.60 | 0.04528 | 41.07 | 0.142 |
| NGC 7196 | -5.0 | 12.31 | 55.66 | 10.73 | 0.192 | 10.500 | 20.05 | 0.05616 | 41.16 | 0.122 |
| NGC 7265 | -3.0 | 13.24 | 104.11 | 11.14 | 1.231 | 11.250 | 45.77 | 0.07785 | 41.93 | 0.087 |
| NGC 7385 | -5.0 | 12.87 | 162.70 | 11.50 | 0.496 | 10.000 | 18.78 | 0.04524 | 42.03 | 0.207 |
| NGC 7454 | -5.0 | 12.80 | 47.00 | 10.48 | 0.616 | 1.230 | 9.65 | 0.02075 | < 40.59 | |
| NGC 7457 | -3.0 | 12.09 | 22.21 | 10.15 | 0.544 | 1.536 | 10.26 | 0.01963 | < 39.92 | |
| NGC 7484 | -5.0 | 12.74 | 54.82 | 10.56 | 0.132 | 1.502 | 9.09 | 0.06196 | < 41.17 | |
| NGC 7507 | -5.0 | 11.36 | 32.07 | 10.72 | 0.270 | 1.571 | 9.05 | 0.16020 | < 41.12 | |
| NGC 7619 | -5.0 | 12.16 | 74.29 | 11.11 | 0.499 | 12.500 | 91.51 | 0.20607 | 42.00 | 0.065 |
| NGC 7626 | -5.0 | 12.15 | 74.29 | 11.11 | 0.499 | 11.250 | 29.50 | 0.06634 | 41.51 | 0.101 |
| NGC 7768 | -5.0 | 13.10 | 164.53 | 11.41 | 0.463 | 10.000 | 15.88 | 0.05374 | 42.11 | 0.136 |
| UGC 4956 | -4.7 | 13.50 | 99.09 | 10.84 | 0.315 | 10.000 | 29.73 | 0.07578 | 41.79 | 0.114 |

Our $L_x$ is consistent with that of the hard component but inconsistent with that of the composite model (lower diamond). In the case of NGC 2300 we measured the emission of the group, which is in good agreement with the value given by PDE (upper diamond), instead of the emission of the single galaxy.

The scatter in the comparison with the luminosities derived by Brown & Bregman (1998, BB) (open circles in Fig. 6) is larger, but the data are still compatible within a factor of 2. The scatter amounts to 0.26 dex. A possible origin of this scatter might be the different approaches to deriving the luminosities. First, BB measured their luminosities in a fixed aperture of $\leq$4 optical half-light radii. Secondly, they fixed the abundance to 50 per cent cosmic, and assumed a two-component model for a fraction of their galaxies. The largest deviation is found for NGC 1399 (central galaxy in the Fornax cluster, left of filled star). This discrepancy might be due to different contributions from the cluster emission. The luminosity measured by Rangarajan et al. (1995) lies in between these two values (filled star).

Most X-ray luminosities plotted in Fig. 6 are deduced by employing measured temperatures and abundances deviating (in some cases by large amounts) from our assumption of 1 keV and $Z = 1$ $Z_\odot$, and/or assuming two-component models. Still, the luminosities on average agree well within a factor of 2, indicating that the overall error of our data is less than 0.3 dex in most cases. The same conclusion can be drawn from the comparison with recent *ASCA* data in the next paragraph.

### *4.2.3 ASCA*

According to Fig. 7, our luminosity agree within a factor of 2 with the *ASCA* results (soft + hard component added up) from Buote & Fabian (1998) (squares) and Matsumoto et al. (1997) (circles). The data are again corrected in the same manner as for the comparison with *Einstein* and *ROSAT* data. The bandpass corrections amount to 0.004 dex for the 0.5–2.0 keV luminosities of Buote & Fabian (1998) and 0.04 dex in the case of the 0.5–4.5 keV data of Matsumoto et al. (1997). Both use a two- (three-) component model fitted to the spectra to derive their X-ray luminosities. The inferred abundances range from $Z_{min} = 0.05$ $Z_\odot$ to $Z_{max} = 2.8$ $Z_\odot$ and the temperatures ranges from $T_{min} = 0.28$ keV to $T_{max} = 1.01$ keV. From this one can again infer that the combined error, arising from the measurement and our model assumptions, is $\leq$0.3 dex.

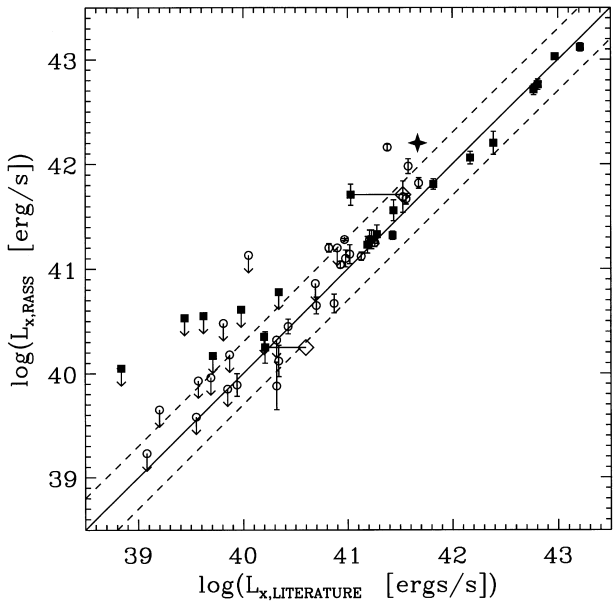


**Figure 6.** Comparison with *ROSAT* X-ray luminosities (pointed observations) compiled from the literature. Filled squares represent data from FKT, FS, J, KF, KFM, PBE, RBK, TFK and TFKC. Open circles indicate data from BB. The filled star refers to the X-ray luminosity of NGC 1399 as measured by Rangarajan et al. (1995). Diamonds are explained in the text. X-ray luminosities are corrected for discordant distance estimates and different energy ranges.

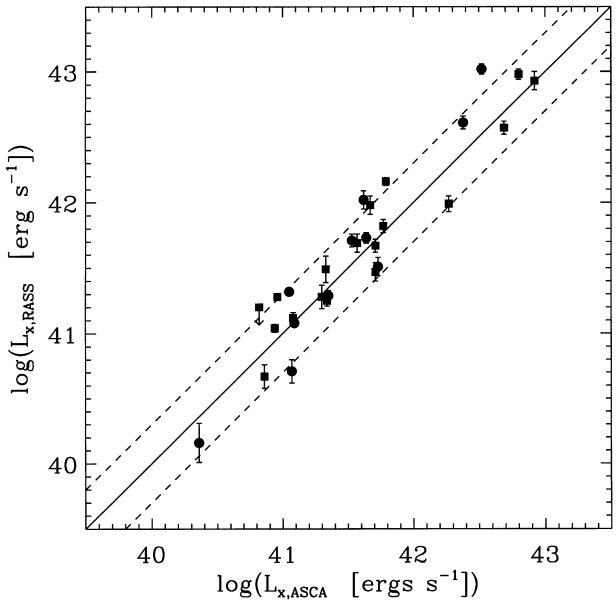


**Figure 7 Comparison with** *ASCA* X-ray luminosities (hard plus soft component) from Buote & Fabian (1998) (squares) and Matsumoto et al. (1997) (circles). Luminosities are corrected for discordant distances and bandpasses. Buote & Fabian (1998) do not give errors for the individual galaxies, but only state that statistical errors are of the order of a few per cent. Matsumoto et al. (1997) only give an error estimate of about 30 per cent for the hard component, which is responsible for only a minor fraction of the total X-ray emission in their observed energy range in most of their galaxies.

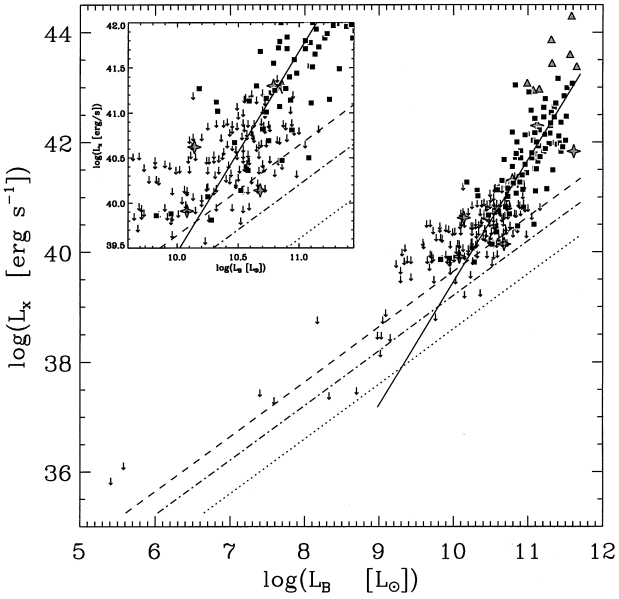


**Figure 8.** Log($L_x$)-log($L_B$) diagram. Open triangles indicate galaxies known to reside at the centres of clusters, filled squares are detections, arrows are upper limits and stars are AGN. Long-dashed, dot–dashed and dotted lines represent X-ray luminosities expected from discrete sources according to CFT, CPR and FJT. The solid line is fitted to the data; see Section 4.4.

### 4.3 Basic properties

The distribution of the data points in the $L_x - L_B$ diagram is shown in Fig. 8. It covers a larger range than the *Einstein* sample. X-ray luminosities range from $\approx 10^{36}$ to $10^{43}$ erg s$^{-1}$, excluding cluster central galaxies. Nevertheless, the latter galaxies at the far bright end of the distribution [$\log(L_x) \gtrsim 43$ erg s$^{-1}$] seem to continue smoothly the distribution to the highest X-ray luminosities. For further discussion see Section 4.5. The lower envelope of the data points is compatible with an amount of discrete emission lying in between the values adopted by Ciotti et al. (1991, CPR) and Forman et al. (1985, FJT), and inconsistent with Canizares et al. (1987, CFT). No X-ray luminosity is found below the limit of Forman et al. (1985), indicating that there exist no early-type galaxies with an unusually low flux from discrete X-ray emitters. Below $\log(L_B) = 9.2$ L$_\odot$ and possibly up to $\log(L_B) = 9.8$ L$_\odot$ the X-ray emission seems to be consistent with, mainly, being due to discrete sources. Between $\log(L_B) = 9.8$ and 11.2 L$_\odot$ a large fraction of galaxies contain gaseous haloes. Above $\log(L_B) = 11.2$ L$_\odot$ no galaxy with only discrete emission is found.

Taking the typical measurement error to be $\lesssim$0.3 dex, the scatter in the diagram is physical and possibly a result of intrinsic variations in the properties of the galaxies, environmental effects or some other as yet unknown influences.

### 4.4 Optical–X-ray correlation

#### *4.4.1 Results for the RASS sample*

Since the data contain upper limits, standard statistical methods cannot be applied. For the purpose of testing the correlation between $L_x$ and $L_B$, the Cox–Hazard model, the modified Kendall $\tau$ test and the modified Spearman rank test, as discussed by Isobe, Feigelson, & Nelson (1986), were used. They yield probabilities that $L_x$ and $L_B$ are not correlated of $P \leq 10^{-4}$ for the whole sample

as well as for parts of it (see below). The only exception is the case for which only galaxies with $L_x \leq 40.5$ erg s$^{-1}$ are considered and where data points are rare. Then the Cox–Hazard test yields $P < 0.004$, while the other two tests again give $P \leq 10^{-4}$.

Linear regression analysis was carried out using the expectation and maximization (EM) algorithm, the Buckley–James (BJ) algorithm and the Schmitt regression (see Isobe et al. 1986). For the EM and the BJ algorithms the uncensored data points were used as independent variables whereas the censored data points acted as dependent variables. In the case of Schmitt's regression the bisector of the fits of (*X/Y*) and (*Y/X*) was taken. Cluster central galaxies were always omitted in this analysis.

Taking the complete data set, the EM method, BJ algorithm and Schmitt binning yield slopes of 2.61(±0.16), 2.58(±0.16) and 1.65(±0.18), respectively, and thus a mean slope of 2.28 with a mean error of ±0.17. The galaxies at the low-luminosity end of the distribution are mainly nearby dwarf galaxies, physically different from the galaxies at the high-luminosity end. Excluding these objects by considering only galaxies with $\log(L_B) > 9.0$ L$_\odot$ indicates a slightly but not significantly steeper slope of 2.41(±0.16).

Our sample contains a larger number of upper limits than detections. Since this may affect the results, we reran the regression analysis, creating sets of data points with equal numbers of detections and randomly selected upper limits. The resulting slopes are slightly shallower, but not significantly. In the case that the nearby dwarf galaxies are included, EM, BJ and Schmitt binning give mean slopes of 2.07(±0.12), 2.06(±0.13) and 1.78(±0.19), respectively, and therefore a mean slope of 1.97(±0.15). If the dwarfs are excluded as described above, the slopes are consistently marginally higher, yielding values of 2.32(±0.14), 2.30(±0.14) and 2.08(±0.10) and thus a mean slope of 2.23(±0.13). This fit is shown in Fig. 8.

We also investigated the luminosity dependence of the relation. A continual decrease of the maximum $L_x$ included in the regression analysis down to 40.5 erg s$^{-1}$ leads to a decrease of the mean slope to 1.04(±0.19). Considering only $L_x \geq 40.5$ erg s$^{-1}$ results in a mean slope of 2.12(±0.15), marginally shallower than the above results. This indicates that it is more suitable to describe the overall distribution as a combination of two relations, one with slopes of ≈1 (consistent with emission from discrete sources), and the other with a slope of ≈ 2 (consistent with the emission from a hot thermal plasma), rather than assigning a single slope to the whole distribution. Moreover, in the latter the use of a linear regression is questionable.

#### *4.4.2 Comparison with previous results*

Our slopes are marginally steeper than but consistent within the errors with the findings of Eskridge, Fabbiano & Kim (1995, EFK), assuming the values derived with equal numbers of detections and upper limits as is the case for the EFK sample. They derived a mean slope of 1.8(±0.14) (mean error) for the complete *Einstein* data set [our results: 1.97(±0.15)] and a mean slope of 2.0(±0.18) excluding the two dwarf galaxies in their sample [our results: 2.23(±0.13)]. Taking the available $D_n$–$\sigma$ distances from Faber et al. (1989) for a subsample steepens the slope to 2.35(±0.25), which is consistent within the errors with all of our results.

BB re-investigated this relationship on the basis of a complete sample observed with *ROSAT*. Their sample comprises 34 optically bright galaxies, avoiding dwarf galaxies (NGC 185, 205, 221) and X-ray-bright quasars (e.g. M87). They derived slopes much steeper than ours. Using the orthogonal linear regression bisector method

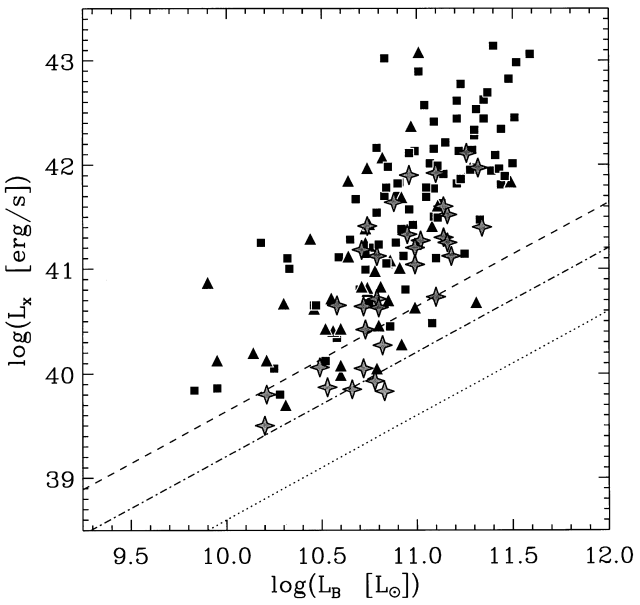


**Figure 9.** Log($L_x$)-log($L_B$) diagram of all detections in our sample except the AGN and the cluster central galaxies (squares), enlarged by the *Einstein* sample (triangles) plus all detections of BB (stars). Data are corrected for different bandpasses and in the latter case to $T = 1$ keV and cosmic abundances (see text).

and excluding one galaxy (NGC 5102), they found a slope of 2.68(±0.25) for the composite X-ray emission (hard plus soft component). This slope is inconsistent with the most reasonable value (since it is not strongly dominated by the statistics of the upper limits) of 2.23(±0.13). If they subtracted the hard component Cen A from the X-ray emission of the sample galaxies, leaving only the gaseous emission, they derived an even steeper slope of 2.96(±0.30). Subtracting the entire emission of Cen A results in a yet steeper slope of 3.51(±0.41). A reason for the discrepancy of slopes may be their limited sample size. Fig. 9 shows the distribution of data points compared with the combined detections of our and the *Einstein* sample. None of their sample galaxies is found below $\log(L_B) \approx 10.6\,L_\odot$ and above $\log(L_x) \approx 40.0$. Using the combined sample yields slopes of less than ≈2.4 in all cases, even when the total bandpass-corrected luminosity of Cen A ($3.57 \times 10^{39}$ erg s$^{-1}$) is subtracted. Although this combined sample is rather badly defined, there are galaxies below $\log(L_B) \approx 10.6$ L$_\odot$ with X-ray luminosities of $\log(L_x) \gtrsim 40.0$ erg s$^{-1}$. When included, they are likely to flatten the slope, as indicated by the combined sample.

### 4.5 Super X-ray-luminous ellipticals

Several models have been developed to explain the X-ray luminosities of early-type galaxies. Besides the overall correlation in the $L_x - L_B$ diagram, the main feature to be explained is the large scatter seen at almost all luminosities.

Steady-state cooling flow models provide an explanation for for some basic properties of the X-ray emission of early-type galaxies (see e.g. Sarazin 1996). However, they suffer from two main problems. First, they predict X-ray luminosities that are far too bright for almost all galaxies at any optical luminosity (solid lines in Fig. 10). This is even true for models with no supernovae at all ($\vartheta_{SN} = 0$). Secondly, there is no obvious explanation for the large scatter in the observed X-ray luminosities among galaxies with equal optical luminosities. Inhomogeneous cooling flow models

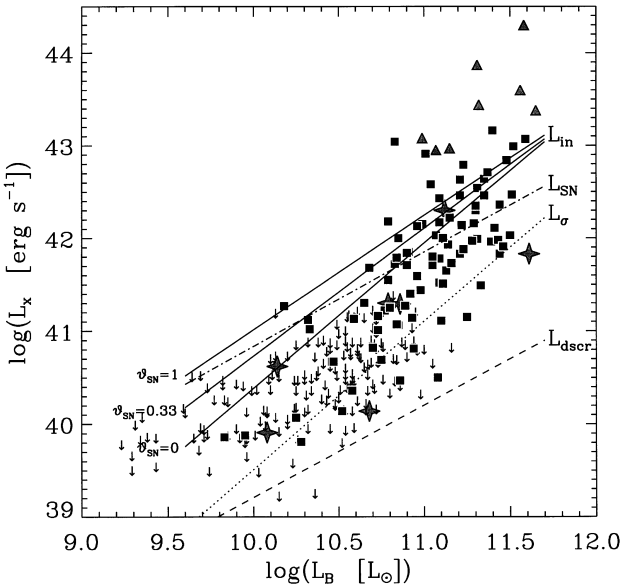


**Figure 10.** Log($L_x$) plotted versus log($L_B$). Symbols have the same meaning as in Fig. 8. Solid lines ($L_{in}$) represent the expected X-ray luminosity of steady-state cooling flow models, taken from CPR, for different supernova rates: $\vartheta_{SN} = 1$ indicates the standard SN I rate (Tammann 1982); $\vartheta_{SN} = 0$ refers to no contribution of SNe I to the heating. The dot-dashed line shows the power $L_{SN}$ generated by the SN I heating at the (present day) standard rate ($\vartheta_{SN} = 1$); the dotted line indicates the heating due to stellar motion ($L_\sigma$); while the dashed line represents the expected contribution from discrete stellar X-ray sources (CPR).

(Sarazin & Ashe 1989) are able to reduce the overluminosity problem by invoking mass drop-out, but they still have problem accounting for the large scatter.

CPR have constructed hydrodynamical evolutionary models (WOI models hereafter). In these models, galaxies can go through up to three different phases. At the beginning they experience a supersonic wind phase, which after a short time turns into a subsonic outflow. The outflow phase is maintained for several Gyr, characterized by a comparatively low X-ray luminosity, until a central cooling catastrophe triggers the transition to the inflow phase with high X-ray luminosities. The scatter in the log($L_x$)-log($L_B$) diagram naturally arises from the fact that the onset of the cooling catastrophe is extremely sensitive to the structural properties of the model galaxies.

The X-ray luminosities expected from present-day heating of Type I supernovae (SNe I) at the standard rate in the WOI models is indicated by the dot–dashed line in Fig. 10. Above $L_B = 10.6\,L_\odot$ an increasing fraction of the X-ray luminosities are in excess of this value. Most of them are consistent with X-ray luminosities expected from the galaxies being in the inflow regime. Indeed, X-ray-bright galaxies observed with *ROSAT* pointed observations, e.g. NGC 507 and 499 (KF), show strong evidence for the presence of cooling flows. Over the whole range of luminosities, approximately 10 per cent of all ellipticals in the X-ray subsample may experience a cooling flow. The true fraction is likely to be smaller since our investigation is based on a magnitude-limited sample and thus has a bias towards optically bright and therefore X-ray-bright galaxies which are the ones that frequently show signs of an inflow. Moreover, the total optical sample is approximately a factor of 2 larger than the X-ray subsample, mainly because a large number of upper limits are omitted as described above. If these omitted galaxies were in the inflow phase they would very probably have been detected. Hence the number of galaxies that are currently not in the inflow phase doubles. This means that the vast majority of all ellipticals ($\gtrsim$95 per cent) are at present in the wind or outflow regime.

Some of the most X-ray-luminous galaxies are brighter than the inflow luminosity $L_{in}$ adopting the standard supernova rate ($\vartheta_{SN} = 1$). Since current estimates of supernova rates in ellipticals are about a factor of 4 lower (Cappellaro et al. 1997), this line can be considered as an upper limit, raising the question of what causes these galaxies to be super-luminous in X-rays. A possible explanation is provided by the observational indication for a smooth transition of the distribution in the log($L_x$)-log($L_B$) diagram from individual galaxies to cluster central galaxies. This suggests that additional gas originating from outside the galaxies could play an increasing role with increasing optical luminosity. The infalling gas would radiate in addition to the gas that is already found in the galaxy. The following facts argue in favour of this interpretation. At high optical luminosities, galaxies are often found to be the brightest member of groups or poor clusters residing at or near their centres. Their deep potential well could allow them to collect group gas or gas from other smaller galaxies via interactions. Accretion from the intracluster medium (ICM) is observed. Mathews & Brighenti (1998) argue that the temperature profile of NGC 4472, which is increasing outwards, requires an accretion of gas from the ICM. We derived approximate gas masses expected from stellar mass loss by integrating the formula given by CPR from 0.5 to 15 Gyr. If one compares these gas masses with the masses of hot gas measured in X-rays, one finds that they are up to about two orders of magnitude lower. Consequently, accreted gas may account for the overluminosity of these galaxies.

## 5 CONCLUSIONS

Based on an optically selected, magnitude-limited sample ($B_T \leq 13.5$ mag) of 530 early-type galaxies, we have constructed an X-ray sample as free of selection biases as possible. We derived X-ray luminosities from the *ROSAT* All-Sky Survey, which provides an ideal basis for such an analysis. The results are 101 detections and 192 useful upper limits in the 0.64–2.36 keV band. Only 68 out of these are included in the *Einstein* sample of Fabbiano et al. (1991). Our data contain a large number of galaxies for which no X-ray data were available until now. The typical measurement error is 0.095 dex. Our X-ray luminosities agree well within a factor of 2 with Fabbiano et al. (1991). The comparison with recent *ROSAT* and *ASCA* data indicates that the overall error in our X-ray luminosities, including measurement errors as well as errors arising from our model assumptions, is $\leq$0.3 dex. Hence the scatter seen in the $L_x - L_B$ plane is real.

The X-ray luminosities for galaxies in this sample range from $10^{36}$ to $10^{43}$ erg s$^{-1}$, excluding cluster central galaxies. No X-ray luminosity is found below the limit of Forman et al. (1985), indicating that there exist no early-type galaxies with an unusually low fraction of disrete X-ray emitters. Below $\log(L_B) = 9.2\,L_\odot$ and possibly $\log(L_B) = 9.8\,L_\odot$, the X-ray emission seems to be consistent with being mainly due to discrete sources. Between $\log(L_B) = 9.8$ and $11.2\,L_\odot$ a large fraction of galaxies contain gaseous halos. Above $\log(L_B) = 11.2\,L_\odot$ no galaxy with only discrete emission is found.

On the basis of our sample we confirm that $L_x$ and $L_B$ are strongly correlated. The slope of the overall $L_x - L_B$ distribution, excluding cluster central galaxies and nearby dwarf galaxies, is found to be 2.23($\pm$0.13), consistent with what is found by Eskridge et al. (1995). We also confirm the luminosity dependence of the relation.

The slope decreases to 1.04($\pm$0.19), lowering the maximum $L_x$ to 40.5 erg s$^{-1}$. Therefore it is more convenient to describe the distribution as a slope $\approx$ 1 section at the low-luminosity end of the distribution, consistent with discrete emission, and a slope $\approx$ 2 section at the high-luminosity end, consistent with gaseous emission.

Comparing the distribution of X-ray luminosities with WOI models (Ciotti et al. 1991), adopting the standard supernova rate, the vast majority of the galaxies ($\gtrsim$95 per cent) are in the wind or outflow phase, leaving only a small fraction that might have experienced the transition to the inflow phase. Some of the latter galaxies are found to be in excess of the X-ray luminosities predicted by cooling flow models with standard supernova rates, which can be considered as upper limits. A possible explanation is suggested by the rather smooth transition of X-ray luminosities from single galaxies towards cluster central galaxies. Accreted gas from outside the galaxies might explain the overluminosity of these galaxies.

## ACKNOWLEDGMENTS

The authors thank the *ROSAT* team of the MPE in Garching. This work was supported by the Deutsche Forschungsgemeinschaft via project Be 1091/6.

## REFERENCES

Allen C. W., 1973, Astrophysical Quantities, 3rd edn. Athlone Press, London
Bender R., Capaccioli M., Macchetto F., Nieto J. 1989, ESO Messenger, 55, 6
Brown B. A., Bregman J. N., 1998, ApJ, 495, L75
Buote D. A., Fabian A. C., 1998, MNRAS, 296, 977
Canizares C. L., Fabbiano G., Trinchieri, G., 1987, ApJ, 312, 503 (CFT)
Cappellaro E., Turatto M., Tsvetkov D. Yu., Batunov O. S., Pollas C., Evans R., Hamuy M., 1997, A&A, 322, 431
Ciotti L., Pellegrini S., Renzini A., D'Ercole A., 1991, ApJ, 376, 380 (CPR)
Davis S. D., White R. E., III, 1996, ApJ, 470, L35
de Vaucouleurs G., de Vaucouleurs A., Corwin H. G., 1976, Second Reference Catalogue of Bright Galaxies. Univ. Texas Press, Austin (RC2)
de Vaucouleurs G., de Vaucouleurs A., Corwin H. G., Buta J., Paturel G., Fouqué P., 1991, Third Reference Catalogue of Bright Galaxies. Springer Verlag, New York (RC3)
Dickey J. M., Lockman F. J., 1990, ARA&A, 28, 215
Eskridge P. B., Fabbiano G., Kim D.-W., 1995, ApJS, 97, 141 (EFK)
Fabbiano G., Schweizer F., 1995, ApJ, 447, 572 (FS)
Fabbiano G., Kim D.-W., Trinchieri G., 1991, ApJS, 80, 531
Fabbiano G., Kim D.-W., Trinchieri G., 1994, ApJ, 429, 94 (FKT)
Faber S. M., Wegner G., Burstein D., Davies R. L., Dressler A., Lyndon-Bell D., Terlevich R. J., 1989, ApJS, 69, 763
Forman W., Jones C., Tucker W., 1985, ApJ, 293, 102 (FJT)
Garcia A. M., 1993, A&AS, 100, 47
Isobe T., Feigelson E. D., Nelson P. I., 1986, ApJ, 306, 490
Jones C., Stern C., Forman W., Breen J., David L., Tucker W., 1997, ApJ, 482, 143 (J)
Kim D.-W., Fabbiano G., 1995, ApJ, 441, 182 (KF)
Kim D.-W., Fabbiano G., Mackie G., 1998, ApJ, 497, 699 (KFM)
Kim D.-W., Fabbiano G., Trinchieri G., 1992, ApJ, 393, 134
Lauberts A., Valentijn E. A., 1989, The Surface Photometry Catalogue of the ESO–Uppsala Galaxies. ESO, Garching bei München
Liedahl D. A., Osterheld A. L., Goldstein W. H., 1995, ApJ, 438, L115
Makishima K. et al., 1989, PASJ, 41, 697
Mathews, W. G., Brighenti F., 1998, ApJ, 495, 239
Matsumoto H., Koyama K., Awaki H., Tsuru T., 1997, ApJ, 482, 133
Matsushita K. et al., 1994, ApJ, 436, L41
Pildis R. A., Bregman J. N., Evrard A. E., 1994, ApJ, 443, 514 (PBE)
Rangarajan F. V. N., Fabian A. C., Forman W. R., Jones C., 1995, MNRAS, 272, 665
Raymond J. C., Smith B. W., 1977, ApJS, 35, 419
Rhee G., Burns J. O., Kowalski M. P., 1994, AJ, 108, 4, 1137 (RBK)
Sandage A. R., 1981, A Revised Shapley–Ames Catalogue of bright galaxies. Carnegie Institution of Washington, Washington DC (RSA)
Sarazin C. L., 1996, in Arnaboli M., Da Costa G. S., Saha P., eds, Proc. Second Stromlo Symp., The Nature of Elliptical Galaxies. Brigham Young, University, Provo, p. 375
Sarazin C. L., Ashe G. A., 1989, ApJ, 354, 22
Tammann G., 1982, in Rees M., Stoneham, R., eds, Supernovae: A Survey of Current Research. Reidel, Dordrecht, p. 371
Trinchieri G., Fabbiano G., Canizares C. R., 1986, ApJ, 310, 637
Trinchieri G., Kim D.-W., Fabbiano G., Canizares C. R. C., 1994, ApJ, 428, 555 (TKFC)
Trinchieri G., Fabbiano G., Kim D.-W., 1996, A&A, 318,361 (TFK)
Trümper J., 1993, Sci, 260, 1769
Tully R. B., 1988, Nearby Galaxies Catalogue. Cambridge Univ. Press, Cambridge
Véron-Cetty M, Véron P., 1996, ESO Scientific Report No. 17, A Catalogue of Quasars and Active Nuclei, 7th edn

This paper has been typeset from a TEX/LATEX file prepared by the author.